

TheraVision: Engineering platform technology for the development of oncolytic viruses based on herpes simplex virus type 1

Christina Funk,¹ Nadja Uhlig,² Zsolt Ruzsics,³ Florentin Baur,⁴ Matthias Peindl,⁴ Sarah Nietzer,^{4,5} Karina Epting,¹ Gabriele Vacun,¹ Gudrun Dandekar,^{4,5} Catherine Botteron,⁶ Christian Werno,⁶ Thomas Grunwald,² and Susanne M. Bailer¹

¹Fraunhofer Institute for Interfacial Engineering and Biotechnology IGB, Stuttgart, Germany; ²Fraunhofer Institute for Cell Therapy and Immunology IZI, Leipzig, Germany; ³Department for Medical Microbiology and Hygiene, Institute of Virology, University Medical Center Freiburg, Freiburg, Germany; ⁴Chair of Tissue Engineering and Regenerative Medicine, University Hospital Würzburg, Röntgenring, Würzburg, Germany; ⁵Fraunhofer Institute for Silicate Research ISC, Translational Center Regenerative Therapies, Würzburg, Germany; ⁶Fraunhofer Institute for Toxicology and Experimental Medicine, Regensburg, Germany

Viruses are able to efficiently penetrate cells, multiply, and eventually kill infected cells, release tumor antigens, and activate the immune system. Therefore, viruses are highly attractive novel agents for cancer therapy. Clinical trials with first generations of oncolytic viruses (OVs) are very promising but show significant need for optimization. The aim of TheraVision was to establish a broadly applicable engineering platform technology for combinatorial oncolytic virus and immunotherapy. Through genetic engineering, an attenuated herpes simplex virus type 1 (HSV1) was generated that showed increased safety compared to the wild-type strain. To demonstrate the modularity and the facilitated generation of new OVs, two transgenes encoding retargeting as well as immunomodulating single-chain variable fragments (scFvs) were integrated into the platform vector. The resulting virus selectively infected epidermal growth factor receptor (EGFR)-expressing cells and produced a functional immune checkpoint inhibitor against programmed cell death protein 1 (PD-1). Thus, both viral-mediated oncolysis and immune-cell-mediated therapy were combined into a single viral vector. Safety and functionality of the armed OVs have been shown in novel preclinical models ranging from patient-derived organoids and tissue-engineered human *in vitro* 3D tumor models to complex humanized mouse models. Consequently, a novel and proprietary engineering platform vector based on HSV1 is available for the facilitated preclinical development of oncolytic virotherapy.

INTRODUCTION

Cancer is a disease that in 2020 affected nearly 10 million people worldwide.¹ Significant progress in cancer treatment has, however, been made with recent developments including oncolytic viruses (OVs)² and immunotherapies.³ Immune checkpoint inhibitors (ICIs)⁴ are therapeutic antibodies developed and already translated into the clinic to overcome the tumor-mediated block of immune

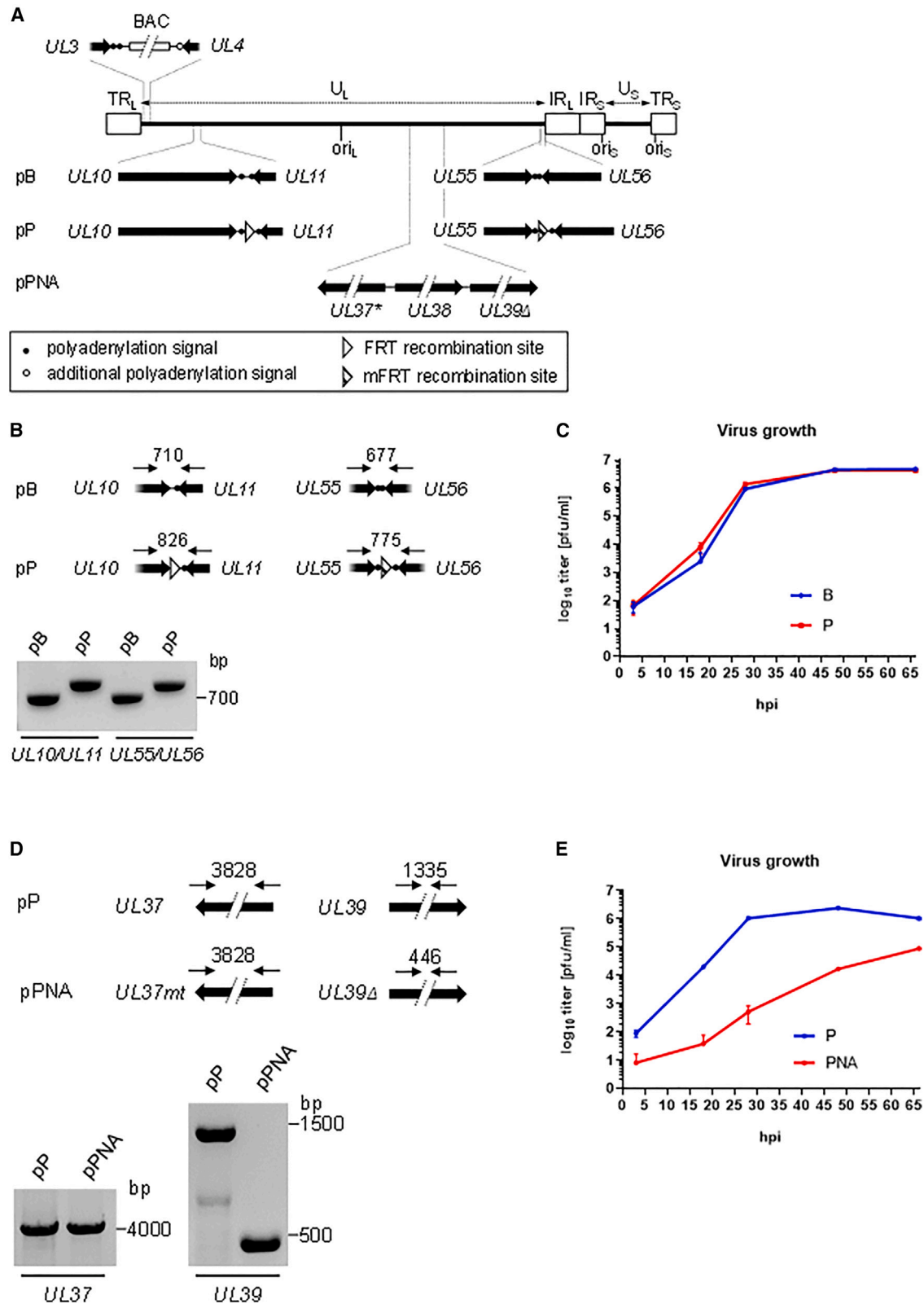
cells, re-enabling the immune cells' ability to fight the tumor cells.^{5,6} OVs, a more recent therapeutic modality for tumor diseases,⁷ multiply upon injection into a tumor, resulting in an inflammatory reaction⁸ with potential long-term effects, a so-called tumor vaccination. Initial results from preclinical and clinical studies of the first and second generation of therapeutic viruses⁹ are highly promising either alone or in combination with other therapeutic modalities such as ICIs.¹⁰

A number of characteristics makes herpes simplex virus type 1 (HSV1) one of the preferred viral vectors for oncolytic virus therapy, while numerous others are currently investigated.^{11,12} Decades of research emphasized therapeutic advantages of the HSV1 vector, such as its replication resulting in cell lysis, the generally self-limiting disease, and an existing and effective antiviral drug.¹³ An HSV1-based OV, called Imlygic or T-VEC, for the treatment of malignant melanoma, was the first OV to receive approval from the Food and Drug Administration (FDA) in 2015. For additional safety, viral replication of T-VEC is controlled by deletion of the infected cell protein (ICP) 34.5.⁹ Further deletion of ICP47 maintains the antigen presentation otherwise downregulated by viral gene products.¹³ Additionally, the virus is modified to express granulocyte-macrophage colony-stimulating factor (GM-CSF) expected to modulate functions of the innate immune system.¹⁴ The approval of T-VEC marks a breakthrough in viral therapeutics with a stimulating effect on the development of new viral technologies and therapies. In the meantime, numerous preclinical and clinical studies using OVs involving T-VEC and a diverse range of viruses are being performed, while translation into the clinic is delayed, suggesting that further improvements of the OVs are necessary.

Received 3 February 2023; accepted 26 February 2024;
<https://doi.org/10.1016/j.omton.2024.200784>

Correspondence: Susanne M. Bailer, Fraunhofer Institute for Interfacial Engineering and Biotechnology IGB, Nobelstraße 12, 70569 Stuttgart, Germany.
E-mail: susanne.bailer@igb.fraunhofer.de





(legend on next page)

Safety and efficacy evaluation of immunomodulating anti-cancer treatments requires complex preclinical models that represent patients' disease and optimally contain the most relevant cells of the tumor microenvironment. Patient-derived preclinical *in vitro* models have been shown to adequately recapitulate drug responses of patients.^{15,16} They can also be combined with relevant immune population such as natural killer (NK) cells or T lymphocytes.^{17,18} As a more complex approach, tissue-engineered human *in vitro* 3D tumor models, such as the porcine decellularized tissue matrix termed small-intestinal submucosa with preserved mucosa (SIS muc) are used. Here, anti-cancer therapies can be investigated in an environment with *in vivo*-like proliferation indices, tissue homeostasis, and physiologic cell anchorage.¹⁹ Co-cultures with non-malignant stromal cells are established on the models,²⁰ also holding the chance to get insight into the specificity of a viral therapy for tumor cells *in vitro*. Further considering the limiting role of the extracellular matrix (ECM) for viral spread, especially in solid tumors with desmoplastic stroma reaction,²⁰ SIS muc models containing the preserved ECM of native tissue hold the capability to model this central aspect for OV therapy. However, most commonly, *in vivo* models such as syngenic mouse models are used to test ICIs, oncolytic viruses, or even the combination of both.²¹ Recently, humanized mouse models have been established²² to evaluate ICI efficacy in a humanized *in vivo* microenvironment.^{23,24}

It was the aim of this project to develop more potent and customized OVs using an effective and high-capacity engineering platform based on HSV1. To this end, we made use of the bacterial artificial chromosome (BAC) technology, a well-established technology for the construction of recombinant herpesviruses.^{25–27} The resulting proprietary engineering platform is characterized by modularity and facilitated integration of several transgenes into the HSV1 genome using recombinational technology. As a proof of concept, transgenes were implemented into the platform vector for optimized targeting and preferential infection of tumor cells on the one hand, and for recruitment and activation of the immune system in the tumor environment on the other hand. Safety and efficacy were evaluated in a novel preclinical testing platform consisting of models with increasing complexity of the tumor microenvironment. These OVs functionalized for a combined virus immunotherapy met the safety

requirements in *in vivo* models, and the virus-encoded targeting molecules specifically infected and lysed the lung tumor cells.

RESULTS

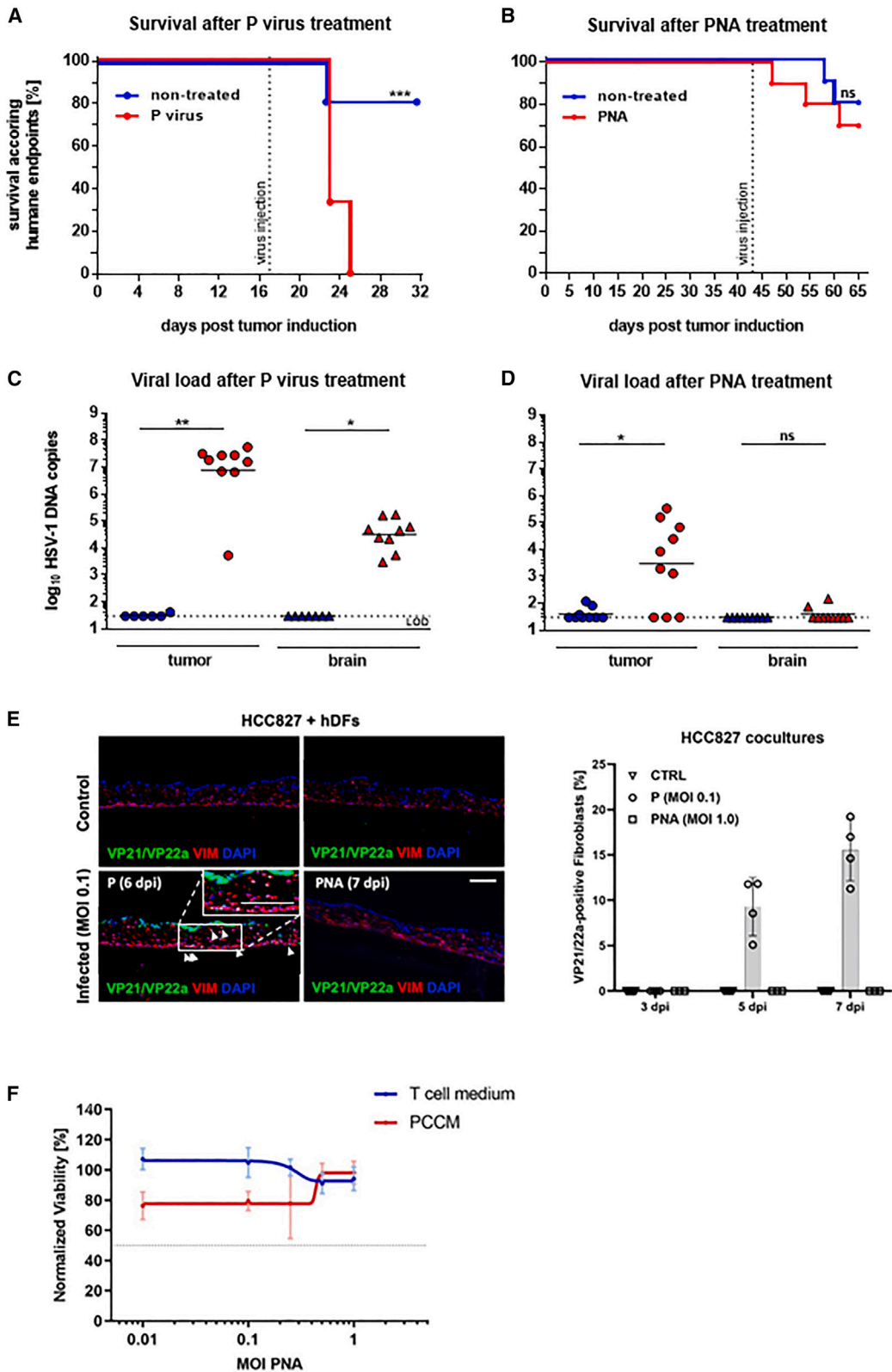
Generation and characterization of an oncolytic platform vector based on HSV1

To develop a highly versatile platform vector based on HSV1, five different clinical isolates were analyzed regarding potency as well as sensitivity against acyclovir and discriminated against HSV2 (data not shown). The most promising isolate was selected to clone the entire HSV1 genome as a BAC using a two-stage genetic manipulation in mammalian cells. To this end, essential bacterial genes together with defined regulatory genes flanked by *loxP* sites were inserted between the herpesviral genes *UL3* and *UL4*.²⁸ As a result, a novel basic vector called pB was available for genetic engineering of HSV1 in *Escherichia coli* (Figure 1A). Viruses reconstituted upon transfection of the pB vector into Vero cells behaved similarly to the selected virus isolate regarding potency and acyclovir sensitivity (data not shown). To allow for an efficient functionalization of the pB vector, the platform vector called pP was created (Figure 1A). In a two-stage process, two different recombination sites, called Flp or flipase recognition target-site (FRT) and mutant FRT (mFRT),²⁹ were inserted between the HSV1 intergenic regions *UL10/UL11* and *UL55/UL56*,³⁰ respectively, of pB. The resulting pP allows for future rapid and targeted insertion of two independent transgene cassettes into pP. The function of both recombination sites was validated by PCR using oligonucleotides to amplify the flanking intergenic regions (Figure 1B) and local sequence analysis; vector integrity was confirmed using restriction fragment-length polymorphism analysis (data not shown). The P virus was reconstituted through transfection of BAC-DNA into Vero cells, thereby essentially all bacterial and regulatory genes between *UL3/UL4* were removed due to the encoded Cre recombinase (data not shown). As a result, only one *loxP* site and an additional polyadenylation signal were left in the viral genome. Growth kinetics of Vero cells infected with the B or P virus at MOI 0.1 were comparable (Figure 1C), indicating that the insertion of FRT/mFRT had no influence on genome stability and viral growth.³⁰

To generate a safe P virus, as required for oncolytic virotherapy, further genetic engineering was applied. To develop a virus selectively

Figure 1. Generation of an oncolytic platform vector based on HSV1

(A) Schematic depiction of the HSV1 genome and the strategy to generate pB, pP, and pPNA vector. To clone the genome of an HSV1 isolate as BAC, essential bacterial genes together with some regulatory elements flanked by *loxP* were inserted between the genes *UL3* and *UL4* creating the basic vector pB. An additional polyadenylation signal derived from *UL21/UL22* of HSV1 was also integrated. Generation of the platform vector pP through insertion of FRT and mFRT recombination sites between tail-to-tail-oriented genes *UL10/UL11* and *UL55/UL56*, respectively, was followed by mutation of *UL37* (*) and partial deletion of *UL39* (Δ) to generate the pPNA vector, an attenuated platform vector with prevented neurotoxicity. Unique sequences (U_L , U_S), inverted terminal (TR_L , TR_S), internal repeats (IR_L , IR_S) and the three origins (ori_L , ori_S) of the HSV1 genome are indicated. Arrows indicate the polarity of each open reading frame. BAC represents essential bacterial genes of pBeloBAC11, Cre cassette, and Zeocin resistance cassette flanked by *loxP* as well as the polyadenylation signal of *UL21/UL22*. (B) To verify the correct insertion of FRT and mFRT recombination sites in order to develop the pP vector, PCR analysis with oligonucleotides flanking the intergenic regions was performed. Expected fragment sizes using two oligonucleotides (arrows) before (pB) and after insertion (pP) are depicted in base pairs. PCR fragments were separated in an agarose gel (2%, TAE) and visualized by Midori Green Advance under UV light. (C) Growth properties of P virus compared to B virus were analyzed by infection of Vero cells with MOI 0.1 in triplicates, harvest of the cell culture supernatant at different hpi, and titration of progeny virus on Vero cells using plaque assay. The error bars represent SD. (D) PCR analysis of genes *UL37* and *UL39* was carried out before (pP) and after genetic engineering steps to create pPNA. Expected fragment sizes using two oligonucleotides (arrows) are indicated in base pairs. PCR fragments were separated in an agarose gel (1.2%, TAE) and visualized by Midori Green Advance under UV light. (E) Growth kinetics of the PNA virus compared to P virus using conditions described in (C).



(legend on next page)

infecting cancer cells, *UL39*, a gene essential for viral replication in non-proliferating cells,³¹ was partially deleted. To remove neurotoxicity of the HSV1 pP vector, the herpesviral tegument protein pUL37, a neuroinvasion effector that facilitates retrograde axonal transport of viral particles,³² seemed promising. Therefore, partial deletion of *UL39* together with targeted mutagenesis of *UL37* were applied to the pP vector in order to generate a neurotox-free and attenuated platform vector called platform, prevented neurotoxicity, attenuation (pPNA). Genetic engineering steps using *en passant* BAC mutagenesis^{33,34} were controlled, among others, by PCR analysis of the concerned regions of *UL37* and *UL39* showing the expected shift of the slower-migrating *UL39* fragment after deletion (Figure 1D). Detailed growth kinetics revealed that replication of the PNA virus was characterized by a rather flat growth curve with no obvious plateau and an overall impairment of about 1 log compared to the P virus (Figure 1E). Thus, growth analysis revealed the attenuation of the PNA virus together with a delayed viral propagation in cell culture. Taken together, a vector for efficient and concerted insertion of two different transgenes via the Flp/FRT system was established and engineered for safe oncolytic virotherapy.

The newly generated platform virus is safe

To investigate the neurotoxic properties of the newly generated pP and pPNA vector, an NSCLC tumor model in NSG mice was used. To this end, luciferase-positive human lung carcinoma cell lines A549^{Luc} and HCC827^{Luc} were generated using lentiviral gene transfer³⁵ allowing for the visualization of cell growth via a highly sensitive camera *in vivo*. Two weeks after subcutaneous application of 2×10^5 bioluminescent cells in immunodeficient NSG mice, palpable tumors had formed. Using bioluminescence imaging, an increase in bioluminescence could be observed in tumors formed by either cell line, which correlated with the increase in tumor volume. Oncolytic virotherapy was performed with a single intratumoral injection of either 1.8×10^7 plaque-forming units (PFU) of P virus or 3.3×10^6 PFU of PNA virus starting at a tumor size of approximately 100 mm^3 (Figures 2A–2D). One week after P virus application, a significant reduction in survival rate (0%, $p < 0.001$) was observed for treated versus non-treated mice (80% survival; Figure 2A), as was expected for the wild-type-like neurotoxicity of the P virus. In contrast, intratumoral injection of PNA virus resulted in survival of treated mice even 3 weeks after virus inoculation, comparable to non-treated ones (Figure 2B), suggesting efficient attenuation of the PNA virus. In addition, successful deletion of neurotoxicity was demonstrated

by detecting ~ 800 -fold less HSV1-DNA in brains of PNA virus versus P virus-treated mice using qPCR analysis (Figures 2C and 2D). Together, this demonstrated that the PNA virus is neurotox free.

To further analyze the selectivity and toxicity/risk of the P and PNA virus, a 3D tissue model derived from porcine intestine (SISmuc) was used representing a complex cellular environment. After seeding SISmuc with human cells in Transwells, a homeostasis-like cell growth is reached within 11 days. Co-cultures of lung carcinoma cells HCC827 with human dermal fibroblasts (HDFs) show a strong infection of both cell types with P virus 6 dpi (MOI 0.1), evident by stained virus proteins in tumor cells on top of the matrix and in single fibroblasts in deeper layers of the matrix (Figure 2E). The P virus exhibited a high potential to eradicate tumor cells with more than 50% 7 dpi (Figure S1). Using the optimized PNA virus, no infection was observed in either fibroblasts or immune cells (THP1) even after 7 dpi and with a 10-fold higher MOI of 1.0 (Figures 2E and S2).

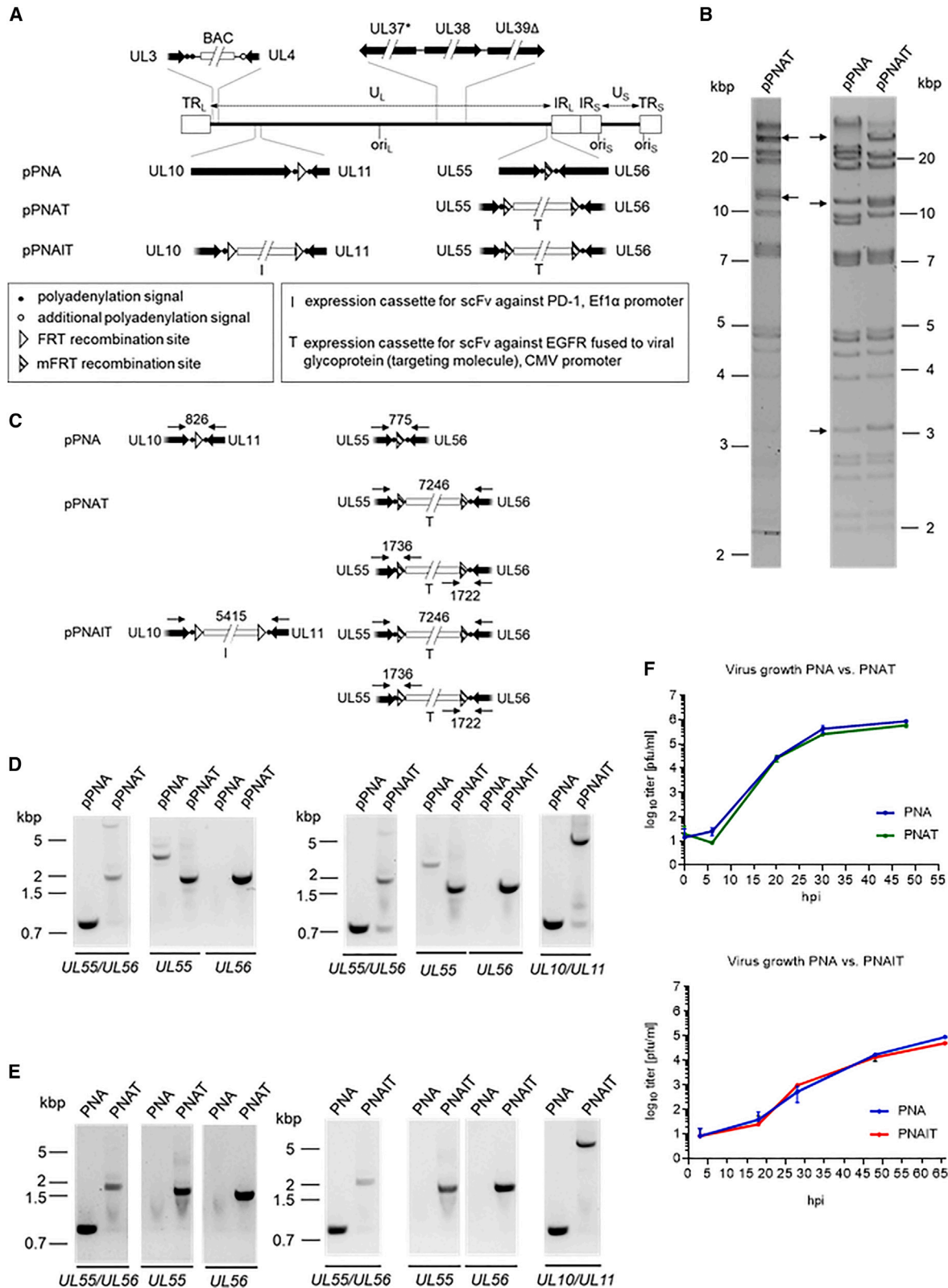
To deepen the insight into the safety of the PNA virus, its impact on non-cancer cells was investigated. Therefore, T cells isolated from peripheral blood were infected with different MOIs for 4 days. As T cells grow under different conditions than cancer cells, the efficacy of the virus was tested in various media (T cell medium, primary cancer cell medium [PCCM]) and under addition of interleukin (IL)-2. No reduction in T cell viability was observed in the tested media over the increased MOI (Figure 2F), supporting the safety of the PNA virus. In addition, the PNA virus demonstrated infection of NSCLC cells with a more advanced and invasive phenotype in SISmuc models (Figure S3). Together, these observations support the successful generation of a selective and safe genetically optimized HSV1 with oncolytic properties.

Virus engineering to develop functionalized OVs against NSCLC

Based on the safe pPNA vector, OVs to specifically kill NSCLC were developed using either one or both recombination sites for insertion of transgenes. The first transgene encoding a targeting molecule was inserted between *UL55/UL56* using mFRT (Figure 3A). Specific targeting of OVs to cells expressing high levels of epidermal growth factor receptor (EGFR) such as NSCLC tumor cells should be achieved by fusion of the HSV1 glycoprotein H to a single-chain variable fragment (scFv) that binds EGFR.³⁶ The second transgene to be inserted between *UL10/UL11* using FRT encodes a myc-tagged antibody fragment scFv that acts as ICI against programmed cell death protein 1 (PD-1) (Figure 3A).

Figure 2. Safety analysis of generated oncolytic platform vectors

(A–D) NSCLC tumor was induced in immunodeficient NSG mice using 2×10^5 A549^{Luc} or HCC827^{Luc} cells on day 0 by subcutaneous injection into the flank and intratumorally treated with 1.8×10^7 PFU of the P virus on day 17 (A and C) or 3.3×10^6 PFU of the PNA virus on day 44 (B and D). (A) and (B) show percentage of survival according to humane endpoints ($n_{\text{non-treated}} = 10\text{--}11$ (blue), $n_{\text{virus}} = 9\text{--}10$ (red)). (C) and (D) show HSV1-DNA copies in tumor (\square) or brain (π) tissue after euthanasia. Statistical analysis was performed by Mann-Whitney U test in comparison to non-treated control. (E) Infection of 3D tissue model of lung carcinoma cells HCC827 cocultured with human dermal fibroblasts (HDFs) 6 dpi. Infection (left) was illustrated by immunofluorescence staining of VP21/VP22a (HSV1 proteins, green). HDFs were visualized by staining of vimentin (red), nuclei by staining with DAPI. White arrows point to double-positive cells (VP21/VP22a, vimentin). Quantitative evaluation of three to five representative pictures (right) shows no infection of fibroblasts by the PNA virus after 3, 5, and 7 dpi. The scale bar corresponds to $100 \mu\text{m}$. (F) T cells isolated from PBMCs were inoculated with increased MOI values of the PNA virus for 4 days in two different media (blue, T cell medium; red, PCCM) before ATP amount was measured. Five replicates were performed for each MOI value. The error bars represent SEM (T cell medium $2 \times 1 \times 5$, 1×4 , PCCM $1 \times 1 \times 5$).



(legend on next page)

Insertion of the transgene encoding a targeting molecule (scFv binding EGFR) between UL55/UL56 using mFRT resulted in the functionalized PNA-targeting molecule PNAT) vector (Figure 3A). Restriction fragment-length polymorphism confirmed expected changes within the pPNAT vector (Figure 3B). Further validation using PCR (Figures 3C–3E) and local sequencing of the transgene region revealed the correct insertion of the transgene. Growth kinetics of the newly functionalized PNAT virus were similar to the PNA virus (Figure 3F). Simultaneous insertion of both transgenes into the pPNA vector resulted in the functionalized (immune checkpoint inhibitor, targeting molecule (pPNAIT) vector. Restriction fragment-length polymorphism confirmed three expected changes within the pPNAIT vector (Figure 3B). Further validation using PCR (Figures 3C–3E) and local sequencing of the transgene region revealed the correct insertion of the transgenes. Growth kinetics of the newly functionalized PNAIT virus were similar to the PNA virus (Figure 3F). Taken together, the results are consistent with the stability of the PNAT and PNAIT virus genome and the tolerance of the viral propagation for inserted transgenes.

The functionalized PNAIT virus was targeted to EGFR-positive cells and expressed a functional PD-1 inhibitor

The PNAIT virus represents a potential oncolytic virus double functionalized by improved targeting via expression of a targeting molecule (scFv against EGFR fused to gH) and expression of an immune checkpoint inhibitor (scFv against PD-1). To analyze the targeting of PNAIT to EGFR-positive cells such as NSCLC tumor cells, a reporter cell assay was applied where EGFR-negative J1.1-2 cells³⁷ were compared to J-EGFR cells that stably express EGFR. To follow the infection of these cells by the PNAIT virus, the herpesviral glycoprotein B (gB) was monitored. As shown in Figure 4A, the PNAIT virus specifically infected J-EGFR but not J1.1-2 cells, and the amount of gB was lower if entry into J-EGFR cells was blocked by anti-EGFR antibodies (Figure 4A). Thus, the PNAIT virus was successfully functionalized for specific recognition of EGFR-expressing target cells.

Expression of the scFv against PD-1 by PNAIT was confirmed in infected cell lysates of both NSCLC cell lines A549 and HCC827 (Figure 4B). The functionality of the virus-encoded scFv was further investigated by a competitive approach involving PD-1 and its ligand partner PD-L1. Using PNAIT virus-infected cell lysates, complex formation between PD-1 and PD-L1 was inhibited by approximately 50%, normalized to the anti-PD-1 antibody pembrolizumab (Fig-

ure 4C). Thus, the virally expressed scFv against PD-1 is functional. Taken together, the double-functionalized virus PNAIT was targeted to EGFR-positive cells and expressed a functional immune checkpoint inhibitor.

The optimized platform virus and the double-functionalized oncolytic virus are potent both on 2D and 3D *in vitro* tumor models

Next, the efficacy of the PNA, PNAI, and PNAIT virus was tested on different NSCLC 2D or 3D *in vitro* models, including a cell line or patient-derived cells. First, a kinetic analysis of viral protein expression throughout viral replication (Figures 5A–5D) was performed in Vero cells infected with PNA (A), PNAI (B), or PNAIT (C) viruses using MOI 0.1 or MOI 5 (data not shown) or mock treated (D). Kinetic analysis of cell lysates revealed that the immune modulating myc-scFv-PD-1 appeared as early as 6 h post infection (hpi) and was prominently detected at 16 hpi upon infection with PNAI and PNAIT viruses (Figures 5B and 5C). As expected, myc-scFv-PD-1 was not observed in cells infected within non-functionalized PNA or mock treated (Figures 5A and 5D). Expression of myc-scFv-PD-1 continued for up to 48 hpi, where co-expression of viral marker proteins indicates the continuous replication of the viruses analyzed. Importantly, the amount and onset of expression of myc-scFv-PD-1 as well as viral marker proteins were comparable in cells infected with either PNAI (expressing myc-scFv-PD-1) or PNAIT (expressing both myc-scFv-PD-1 as well as the targeting function), indicating that virus efficacy was unaffected by double functionalization (Figures 5B and 5C). Similar results were achieved upon infection of Vero cells with PNAI or PNAIT at MOI 5 (data not shown). Taken together, these comparative kinetic data showed a robust and persistent expression of the immunomodulatory scFv-PD-1 by single- or double-functionalized PNAI or PNAIT viruses revealing a wide window for their application in oncolytic virotherapy in terms of time and MOI.

Next, killing curves on lung carcinoma cell lines HCC827 and A549 were performed. The PNAIT virus was able to reduce the cell viability to 55.3% for HCC827 (Figure 5E) and even to 43.7% for A549 (MOI 0.5) (Figure 5F) showing a trend similar to the PNA virus.

As a proof of concept, both viruses—PNA and PNAIT—were tested on 2D and 3D patient-derived models. Both the PNA and PNAIT virus led to similar 50% MOI values on the 2D and even 3D model. For the 2D model, the calculated 50% MOI of the PNA and PNAIT virus

Figure 3. Transgene insertion to develop the functionalized OVs PNAT and PNAIT

(A) Schematic depiction of the transgene insertion by Flp-mediated recombination. The transgene encoding a targeting molecule (scFv against EGFR fused to gH) between UL55/UL56 via mFRT resulted in the functionalized pPNAT. The transgene encoding an immune checkpoint inhibitor (scFv against PD-1) was inserted between UL10/UL11 via FRT, resulting in the double-functionalized pPNAIT vector. (B) To analyze restriction fragment-length polymorphism of the pPNAT and pPNAIT vectors compared to the pPNA vector, isolated BAC-DNA was digested with NotI, separated in 0.8% TBE agarose gel and visualized by Midori Green Direct under UV light. Arrows point to important differences. (C–E) Insertion of transgenes was verified by PCR analysis using oligonucleotides flanking the intergenic regions before (pPNA) and after functionalization (pPNAT and pPNAIT). In (C), oligonucleotides are shown as arrows. Expected fragment sizes are indicated in base pairs. In (D) PCR analysis was done using isolated BAC-DNA as template. (E) Fragment analysis using nucleic acids of reconstituted virus as template. (D and E) PCR fragments were separated in an agarose gel (1.2%, TAE) and visualized by Midori Green Advance under UV light. (F) To analyze growth kinetics of the PNAT and the PNAIT virus compared to PNA virus, Vero cell were infected with MOI 0.1 in triplicates. Progeny virus at different hpi in the supernatant were detected using plaque assay.

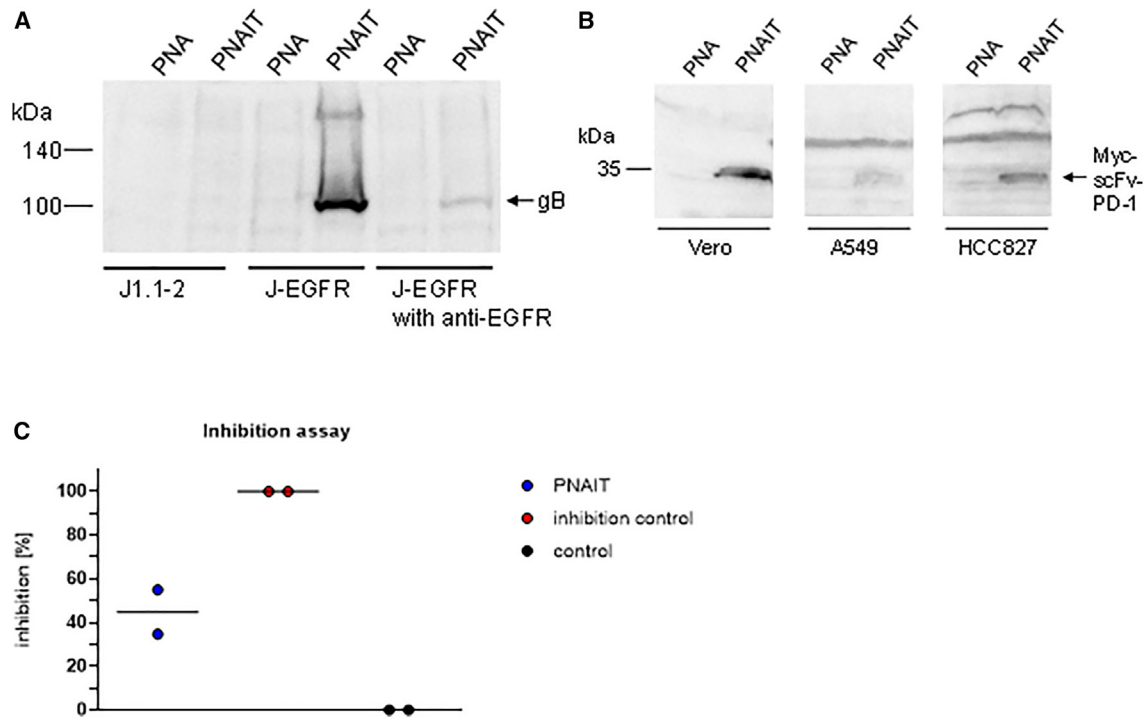


Figure 4. Functionality test of PNAIT virus-encoded targeting molecule and immune checkpoint inhibitor

(A) Targeting of the PNAIT virus to EGFR-expressing cells was analyzed through a cell-based assay using J1.1-2 cells and derivatives (J-EGFRs) that are deficient for wild-type HSV1 infection. J1.1-2, J-EGFR, and J-EGFR cells with blocked EGFR via anti-EGFR antibodies were incubated with the PNA or PNAIT virus, lysed 20 hpi, and analyzed by SDS-PAGE and western blot using anti-gB antibodies. HSV1 gB representing a successful penetration is indicated by an arrow. (B) Virus-encoded expression of scFv-PD-1 was investigated after infection of Vero, A549, and HCC827 cells with the PNAIT or PNA virus as control. Cell lysates were harvested 20 hpi and analyzed via SDS-PAGE and western blot using anti-Myc antibodies. Myc-scFv-PD-1 is indicated by an arrow. (C) To test the functionality of scFv-PD-1, PNAIT virus-infected Vero cell lysate was analyzed in a PD-1:PD-L1 inhibitor assay. Inhibition was normalized to the inhibition control, anti-PD1 antibodies (100 nM). Untreated cell lysate was used as control (n = 2).

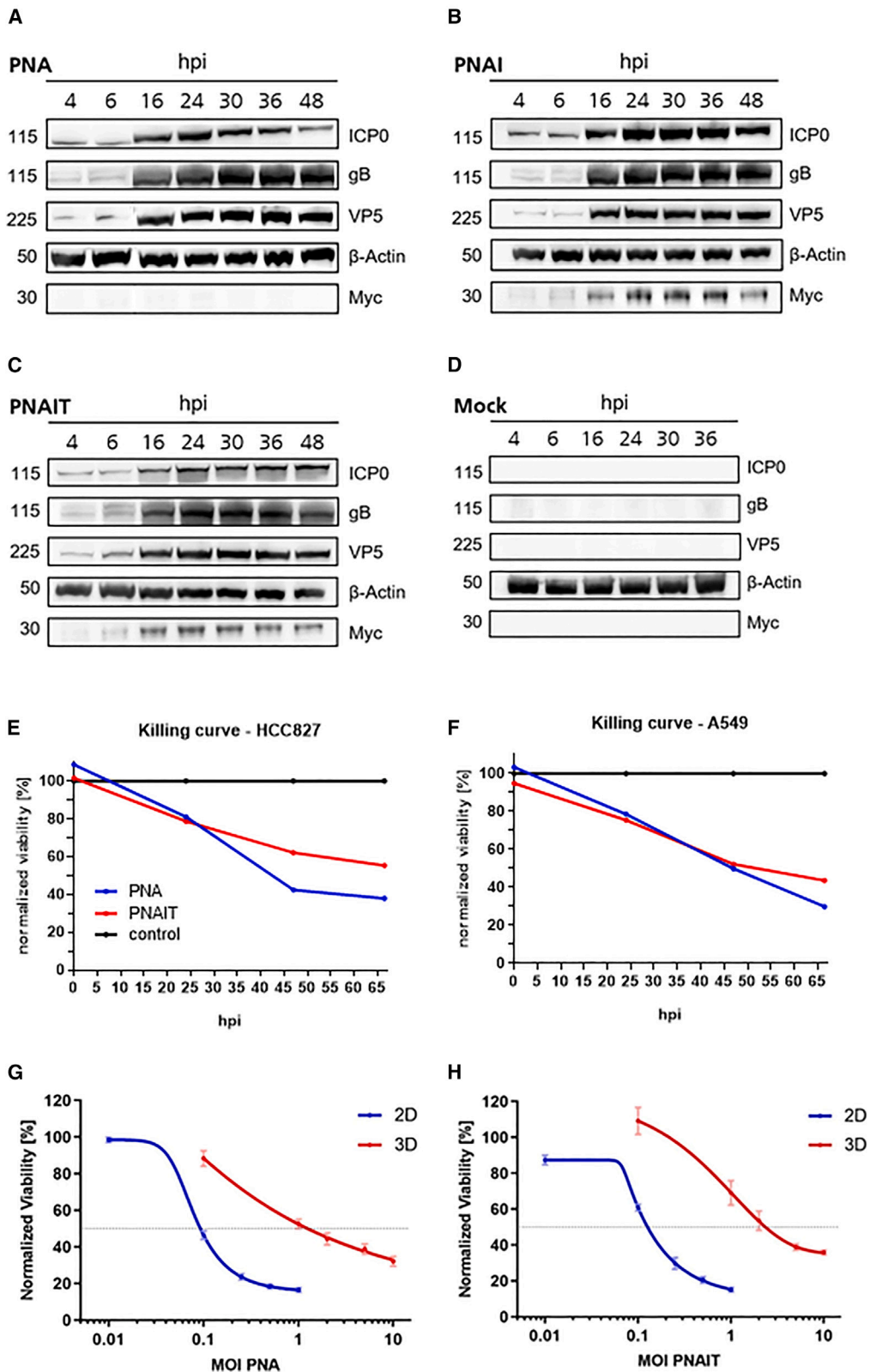
was 0.111 ± 0.012 and 0.141 ± 0.019 , respectively (Figures 5G and 5H). For the organoids, the 50% MOI of the PNA and PNAIT virus was 1.959 ± 0.524 and 2.159 ± 0.366 , respectively (Figures 5G and 5H). These results suggest a reliable efficacy of the PNAIT virus on 2D and even 3D *in vitro* models, equipped with patient-derived tumor cells. Taken together, the efficacy of the optimized platform virus and the functionalized PNAIT virus could be demonstrated on distinct *in vitro* NSCLC models.

The oncolytic virus reduced NSCLC growth in a mouse *in vivo* tumor model, a trend confirmed in humanized mice

To compare the oncolytic effects of the PNA virus and the functionalized PNAT and PNAIT viruses on tumor progression, oncolytic virotherapy was performed in an NSCLC tumor model in humanized NSG mice (Figure S4A). PNA virus was administered on day 43 after tumor induction by single intratumoral injection of 3.3×10^5 PFU, while the control group remained untreated. Prior to virus application, both groups exhibited comparable tumor growth (Figure 6A). Immediately after PNA virus treatment, significant inhibition ($p < 0.05$) in tumor progression was observed. In contrast, the tumor of the non-treated control group increased by a multiple of the initial volume. During the first 2 weeks after virus injection (day 44 to day

58), tumor growth was arrested without an increase in mean tumor volume. In the course of the experiment, the tumor volume increased again in virus-treated mice but did not achieve volumes comparable to non-treated tumors 3 weeks after oncolytic virotherapy. Comparable findings regarding tumor progression were obtained by analysis of tumor bioluminescence (Figure 6B, exemplary image). Oncolytic virotherapy using the PNA virus showed an inhibited increase in bioluminescence 20 days after treatment induction compared to non-treated tumors (Figure S4). Explanted tumors were examined by immunohistochemistry, showing PNA-treated tumors with multiple HSV1-positive areas (Figure 6C). Clusters of HSV1- and TUNEL-positive areas (detection of apoptosis-induced fragmented DNA) suggest virus-induced apoptosis processes, detectable only in PNA-treated tumors.

Since efficient inhibition of tumor progression was demonstrated for single PNA virus application in the bioluminescent tumor mouse model, triple intratumoral application (3.3×10^5 PFU each) of the PNAT virus at 1-week intervals was investigated in comparison to a single injection. All groups showed comparable tumor growth until initial virus inoculation on day 53 (Figure 6D). Triple administration of the targeted PNAT virus showed significant inhibition of tumor



(legend on next page)

growth compared to the untreated control group ($p < 0.05$). This effect was sustained, resulting in long-term suppression of tumor progression. Interestingly, comparable results could be obtained even with a single dosage of the PNAT virus. Furthermore, a significant increase in survival to $\sim 50\%$ ($p < 0.05$) was demonstrated using triple PNAT virus application in contrast to the non-treated control group with 0% survival (Figure 6E). Upon single treatment, $\sim 30\%$ of mice survived. In addition, the clinical score was significantly increased in non-treated animals (single therapy, $p < 0.01$; triple therapy, $p < 0.05$), referring to tumor size (Figure S5). No adverse effects attributable to HSV1 infection were detected in any treated mouse.

Since efficacy evaluation of the functionalized PNAIT virus requires the presence of immune cells, immunodeficient NSG mice were humanized prior to tumor induction. After formation of HCC827^{Luc}-derived tumors, intratumoral treatment with 1.6×10^5 PNAIT virus was performed and compared to an untreated control group. PNAIT virus-treated mice showed tendential reduction regarding tumor progression compared to untreated tumors with unaffected tumor growth (Figure S6). The tumor-inhibitory effects were long lasting and did not require further application of oncolytic virotherapy.

DISCUSSION

With the project TheraVision, a broadly applicable engineering platform technology for a combined virus immunotherapy was successfully established. First, the entire workflow for BAC cloning of viral genomes has been established, available to efficiently clone the genome of any viral isolate and to transfer it into a platform vector. Using this technology, a novel and proprietary oncolytic vector for recombinational engineering was developed based on HSV1. Safety, efficacy, and specificity of the functionalized viruses have been evaluated in a novel preclinical testing platform ranging from patient-derived organoids and tissue-engineered human *in vitro* 3D tumor models to animal models that enable analysis of tumor-immune interactions. Overall, a novel, efficient, and meaningful workflow for the preclinical development of an oncolytic virotherapy is available.

To establish and modify the engineering platform, the BAC technology that allows for cloning of entire large viral genomes and their genetic manipulation was applied.²⁵ Compared to other viral engineering approaches that mostly use cell-based modifications, the BAC technology is performed in the bacterial system using *E. coli* genetics and thus completely independent of cellular and viral parameters that vary in the course of viral infection. Importantly, the BAC technology

can be complemented by other engineering technologies, such as CRISPR-Cas.³⁸ In this study, a highly potent clinical isolate was cloned as BAC, which is now available for traceless and precise genetic modification of the viral vector independent of the cellular context.

Using this novel HSV1-BAC, two genomic sites were predefined on the basic BAC vector for recombinational integration of transgenes. These include the long-known FRT and mFRT sites that differ in sequence.^{29,39,40} Importantly, in contrast to previous OVVs, this novel platform allows for a controlled integration of transgenes with the integrity and expression of the herpesviral genome being maintained.¹³ As proof of concept, two different transgenes, one for retargeting of the virus, the other for expression of an ICI, were integrated simultaneously to generate the pPNAIT. Together, these transgene cassettes amounted to roughly 2×4 kb, significantly extending the size of the viral genome. We demonstrate the site-specific insertion and integrity of both transgene cassettes. Consistently, double-functionalized virus with infectious properties comparable to the predecessor virus could be reconstituted. Thus, the TheraVision vector tolerates significant amounts of foreign genetic information and is thus amenable to high-capacity programming. Interestingly, with a developing time of just a few weeks from design to transgene insertion and viral testing, this modular and recombinational engineering platform is highly suitable as high-throughput research platform for transgene development and testing.

Specific targeting of the virus to cancer cells was achieved by one transgene expressing glycoprotein H fused to an EGFR-specific scFv recapitulating recent developments.³⁶ Indeed, the resulting virus specifically infected cells overexpressing EGFR demonstrating the functionality of the HSV1-exposed targeting molecule. The second transgene aimed at enhanced efficacy of the oncolytic virus, encoding an scFv against the immune checkpoint PD-1. Expression and functionality of the PD-1 inhibitor was confirmed in lysates of infected tumor cells. Interestingly, all attempts to detect the virally encoded ICI in the extracellular milieu remained unsuccessful. Our findings suggest that the ICI had entered the secretory pathway where it was processed into a functional component, unstable upon release to the extracellular milieu. We thus conclude that the virally encoded ICI is functional but its effect may be strongest in close proximity to the infected tumor cell.

To generate a viral vector and HSV1 virus that, in addition to being sensitive to the antiviral acyclovir, satisfies all safety requests, the

Figure 5. Efficacy of the safe PNA virus and the functionalized PNAI and PNAIT virus on different 2D and 3D *in vitro* models

(A–D) Kinetic analysis of viral protein expression throughout viral replication was performed in Vero cells infected with PNA (A), PNAI (B), or PNAIT (C) viruses using MOI 0.1 or mock treated (D). Cell lysates were harvested at 4, 6, 16, 24, 30, 36, or 48 hpi and analyzed via SDS-PAGE and western blot using antibodies detecting ICPO, glycoprotein gB, or VP5, viral marker proteins of the immediate-early, early, or late transcriptional phase, respectively. A myc-specific antibody was used to follow the kinetic expression of the immune modulating myc-scFv-PD-1. As loading control, the cellular protein β -actin was detected. (E and F) Killing curves of PNAIT compared to PNA on HCC827 (E) and A549 (F) carcinoma cell lines were performed over 66.5 hpi (MOI 0.5). Cell viability was measured using neutral red assay. Values were normalized on the mock-infected/untreated control. (G and H) For efficacy testing of PNA (G) and PNAIT (H) on NSCLC patient-derived models, the 2D model (blue) was inoculated with MOI value between 0.01 and 1 while the 3D model (red) was inoculated with MOI values from 0.1 to 10. The ATP counts were normalized on the untreated control. Five replicates were performed for each MOI value, and the experiments were repeated at least twice. The error bars represent SEM.

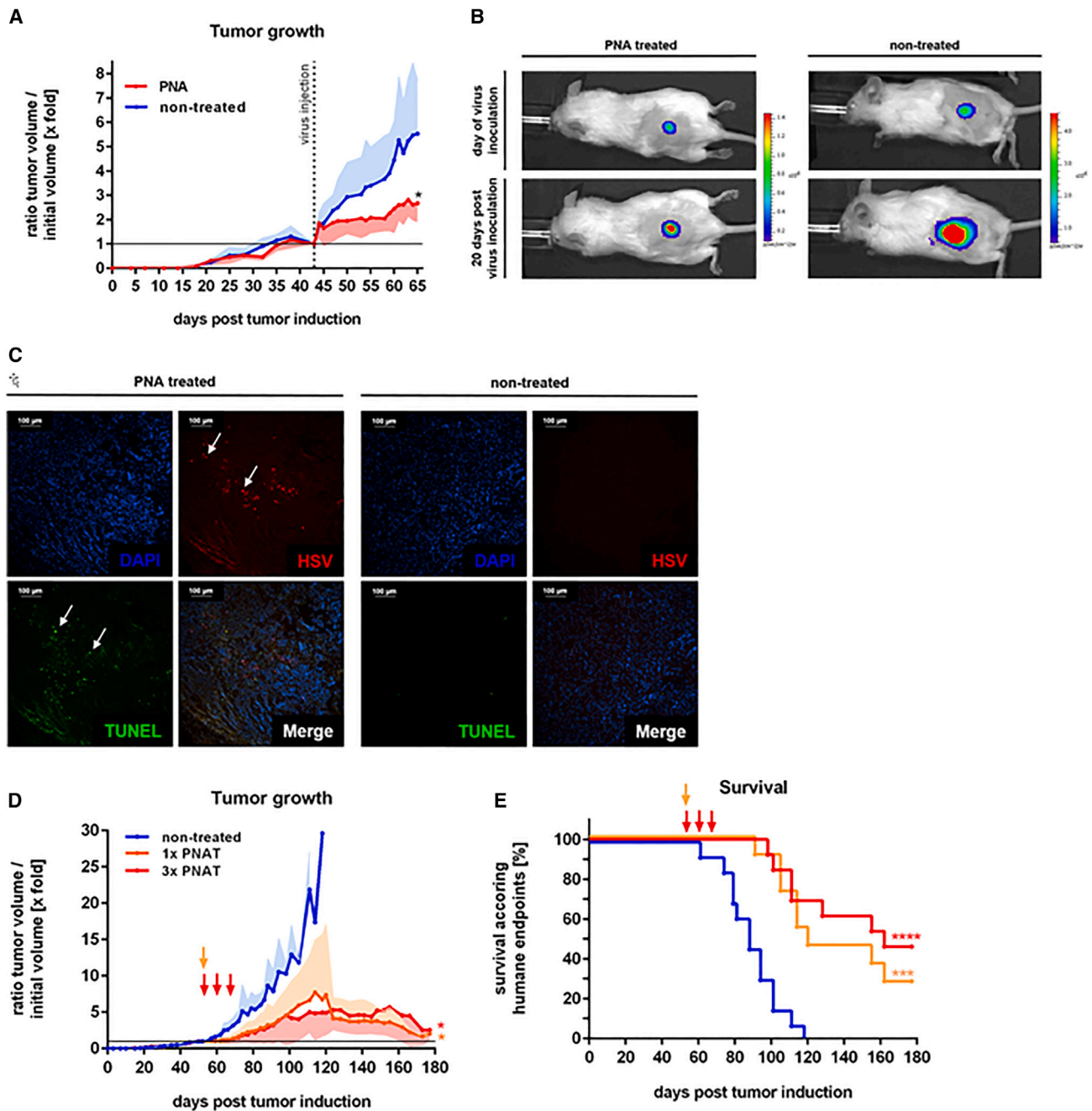


Figure 6. Efficacy of the platform and functionalized oncolytic virus on 3D *in vivo* model

(A–C) NSCLC tumor was induced in immunodeficient NSG mice using 2×10^5 HCC827^{Luc} cells on day 0 by subcutaneous injection into the flank and intratumorally treated with 3.3×10^6 PFU of PNA on day 44. (A) Tumor progression of non-treated (blue) or PNA-treated (red) mice ($n = 10$) compared to initial tumor volume on day 44. (B) Tumor bioluminescence in mice 20 dpi compared to initial tumor bioluminescence. (C) Tumor tissue sections with immunofluorescence staining against HSV1 capsid proteins (VP5, red) from non-treated and PNA-treated tumors. The cell nuclei were stained with DAPI. Apoptosis-induced fragmentation of DNA was visualized using TUNEL method (green). White arrows point to clusters of HSV- and TUNEL-positive regions. The scale bar corresponds to 100 μ m. (D and E) NSCLC tumor was induced in immunodeficient NSG mice using 2×10^5 HCC827^{Luc} cells on day 0 by subcutaneous injection into the flank and intratumorally treated once with 3.3×10^6 PFU of PNAT on day 53 ($n = 11$, orange). Another group received PNAT intratumorally three times at 7-day intervals ($n = 13$, red). Additionally, a non-treated tumor group was included as control ($n = 13$, blue). (D) Percentage of survival according to humane endpoints. (E) Tumor progression compared to initial tumor volume on day 53. Statistical analysis was performed by Mann-Whitney U test in comparison to non-treated control.

platform vector was further modified by partial deletion of the essential viral gene *UL39* (encoding ICP6, the large subunit of ribonucleotide reductase [RR]) with the aim to provide a virus that selectively replicates in highly proliferating cells such as cancer cells while sparing non-proliferating ones.³¹ Neurotoxicity of the HSV1 pP vector was addressed by targeted mutagenesis of *UL37*, a gene encoding the herpesviral tegument protein and neuroinvasion effector pUL37.³² Growth kinetics of the engineered virus showed its attenuation, and the increase in safety was demonstrated by a significant increase in survival of animals infected with the *UL37/UL39* modified virus compared to the wild-type one. The dramatic reduction of HSV1-DNA in brains of mice infected with the modified virus further demonstrated the successful removal of neurotropism and thus neurotoxicity of the modified virus. Remarkably, mutagenesis of the tegument protein pUL37 represents a novel, minimalistic, and effective principle to remove viral neurotoxicity that also marks a notable difference to T-VEC.¹³ Taken together, the resulting innovative vector was shown to be attenuated, neurotox free, and suited for virotherapy based on its increased safety profile.

Oncolytic virotherapy primarily focuses on therapy of solid tumors where it initiates a highly complex inflammatory process, including viral propagation, tumor cell destruction, attraction, and stimulation of immune cells.^{8,41} However, preclinical safety and efficacy evaluation of OV is generally still performed in conventional 2D and immunodeficient animal models. Despite lacking a human microenvironment, the latter have provided profound knowledge on efficacy and safety of OVs and their combination with ICIs.^{42,43} In TheraVision, we have established a complex test platform including patient-derived models, 3D tissue models, as well as humanized mouse models enabling OV testing in an appropriate time frame. Initially, efficacy of the engineered viruses was shown in 2D cell lines as well as patient-derived organoid models that recently have been shown to provide meaningful preclinical data to test efficacy of OVs.⁴⁴ However, whether co-cultures of organoids and autologous immune cells can be used to model OV-dependent immune activation needs to be evaluated. Furthermore, the optimized OV candidates are investigated in novel tissue-engineered 3D tumor models integrating cues from the microenvironment such as tissue architecture, ECM components, and also stromal cells. In the tissue-engineered Transwell-model tumor, cell growth of several entities, such as colorectal, breast, and lung cancer, is sustained with microphysiological characteristics,^{19,45,46} and immune-therapeutic approaches such as CAR T cells^{47,48} and trispecific antibodies¹⁹ can be evaluated. Co-culturing HSV1-permissive fibroblasts⁴⁹ with tumor cells on the SISmuc allowed a risk assessment of the viral therapy *in vitro* that was in agreement with the *in vivo* models in this study. The abolished infection of fibroblasts with the attenuated virus went, however, hand in hand with reduced oncolytic effects on the 3D models, asking for optimization including higher doses for effective therapy.⁵⁰ Furthermore, we tested the functionalized PNAIT in humanized mice in presence of human immune cells, confirming the long-lasting tumor-inhibitory effects. Since humanized mice have previously been used for evaluation of ICI efficacy,^{23,24} it seems reasonable to assume

that immune activation by OVs or in combination with ICI can also be adequately represented in those models. However, the full immune-activating potential of engineered virus in humanized mouse models needs to be further evaluated in future.

By combining information from several preclinical models ranging from patient-derived organoids, tissue-engineered human 3D tumor models, and humanized mouse models, we aim to represent the most relevant components of the tumor microenvironment to characterize OV efficacy. Perspectively, additional efforts are required, e.g., to determine the immunostimulating activity of OVs; their ability to penetrate the tumor; and, most importantly, their potential to act as long-lasting tumor vaccines in models that fully recapitulate the complexity of tumor microenvironments and specific tumor types.^{51,52} Therefore, further developments are required toward more meaningful preclinical models, e.g., by integrating human tissue-derived models⁵³ such as tissue slice cultures into our pipeline to successfully translate OV therapy concepts into the clinical situation.

Oncolytic engineering platforms are of high importance for further improvement of therapy combinations in cancer.⁵⁴ Besides the introduction of checkpoint blockade options as addressed here, OV therapy could be combined with standard-of-care therapeutics. In contrast to the already approved T-VEC, the TheraVision vector represents an innovative open platform for versatile engineering and thus (combinational) treatment of varying types of cancer in a personalized manner. TheraVision can be modularly programmed to encode varying functions for enhanced efficacy and specificity of OVs. Future clinical trials where systemic or intratumoral co-application of, e.g., ICIs with OVs is compared to effects of OV-encoded ICIs may provide interesting insights into pros and cons of these different approaches.

While the antitumor effect of viruses was discovered more than 100 years ago,⁵⁵ the breakthrough in oncolytic virotherapy only came in 2015/2016 with the approval of T-VEC: more than 97 clinical trials were performed between 2000 and 2022, with promising results.⁵⁶ Considering the intense developments of the last years, further FDA approvals are expected to follow soon, accompanied by an enormous upswing in this form of tumor therapy. Still, OVs reach the market with a delay hampered by insufficient specificity, efficacy, and safety. With the workflow developed by TheraVision and presented in this study, we are prepared to significantly contribute to advanced development, approval, and translation in the field of oncolytic virotherapy.

MATERIALS AND METHODS

Cells

Vero (ATCC no. CCL-81), HCC827 (DSMZ ACC566), HCC44 (DSMZ ACC534), A549 (DSMZ ACC107), THP1 (DSMZ ACC16), adult HDFs (HDFa), Gibco C0135C), and J1.1-2 cells (kindly provided by G. Campadelli-Fiume, University of Bologna, Bologna, Italy) were cultured at 37°C and 10% CO₂ under humid atmosphere.

J-EGFR cells were generated by transfection of J1.1-2 cells with the plasmid pCAGGS-SM2667 followed by puromycin (5 µg/mL) selection.

Construction of plasmids

Newly assembled plasmids were controlled by restriction digest and local sequence analysis (Eurofins Genomics, Ebersberg, Germany). The plasmid pMA-SM2274 was assembled through insertion of the cloning fragment in pMA via PacI/AscI by Invitrogen (Thermo Fisher Scientific, Waltham, MA). The cloning fragment was assembled from synthetic oligonucleotides and/or PCR fragments and can be excised by NruI-ScaI restriction. It contains the GFP cassette of pEGFP-N1 (nt 5–1,642, GenBank: U55762) (Clontech Laboratories by Takara Bio USA, San Jose, CA) followed by the polyadenylation site of *UL21/UL22*⁵⁷ of human herpesvirus 1 strain 17 (nt 43,661–43,930, GenBank: JN555585.1), flanked by parts of BamHI to mimic insertion into the intergenic region of *UL3/UL4* via BamHI⁵⁸ and additionally flanked by sequences of about 2 kbp up- and downstream of the intergenic region of *UL3/UL4*.

To remove one SphI restriction site in the gene *lacZ* and to insert two restriction sites up- and downstream of the *lacZ* expression cassette (PciI and SphI), the vector pSF-CMV-BetaGal (Sigma-Aldrich, Merck, Darmstadt, Germany) was rearranged using Gibson Assembly cloning (NEB, Ipswich, MA) and oligonucleotides no. 1–6 (Table 1). Incorporated mutations were controlled through Sanger sequencing with oligonucleotides no. 7–9 (Table 1). The resulting plasmid was named pSF-SM2464.

pEX-A128-SM2334, which contains one *loxP* site flanked by homologous sequences for further cloning, was synthesized by Eurofins Genomics (Ebersberg, Germany).

pUC19-SM2466 was cloned using Gibson Assembly cloning and contains one *loxP* site and sequences of about 2 kbp up- and downstream of the intergenic region of *UL3/UL4*. Fragments were generated by PCR using oligonucleotide no. 10/11 (Table 1) and pMA-SM2274, oligonucleotide no. 12/13 (Table 1) and pMA-SM2274, oligonucleotide no. 14/15 (Table 1) and pEX A128-*lox-syn* as well as oligonucleotide no. 16/17 (Table 1) and pUC19. Correct cloning was controlled using sequencing oligonucleotides no. 18–20 (Table 1).

To assemble the plasmid pBeloBAC11-SM2465 that contains the *lacZ* expression cassette in pBeloBAC11, the SphI/PciI and PciI/SphI fragment of pBeloBAC11 (NEB, Ipswich, MA) and pSF-SM2464, respectively, were ligated using ElectroLigase (NEB, Ipswich, MA).

The plasmid pBeloBAC11-SM2467 was cloned by ligation of the SphI/BstEII fragment of pBeloBAC11-SM2465 and the BstEII/SphI fragment of pUC19-SM2466. pBeloBAC11-SM2467 contains the *lacZ* expression cassette and the SphI/PciI fragment of pBeloBAC11 containing bacterial genes *SopABC* for active partitioning, *ori2* as origin of replication, *RepE* as initiation factor for replication, and the chloramphenicol resistance gene for selection. The assembled sequences are

flanked by *loxP* sites, further flanked by sequences of about 2 kbp up- and downstream of the GFP cassette of the fluorescently labeled HSV1. The plasmid pBeloBAC11-SM2467 can be linearized by PmlI.

The plasmid pUC19-SM2479 contains one *loxP* site, the Cre cassette with a synthetic intron preventing expression of the functional protein in *E. coli* from pCREin⁴⁹ and the Zeocin resistance cassette (nt 1–645) from pOriR6K-*zeo-ie*.⁵⁹

The donor plasmids for transgene insertion via FRT/mFRT²⁹ were cloned using Gibson Assembly based on pGPS-CMV/GFP-Kn-FRT (GenBank: MT731686) and pGPS-CMV/GFP-Kn-mFRT,²⁵ respectively. The donor plasmid pGPS-SM2532 corresponds to pGPS-CMV/GFP-Kn-FRT (nt 1–2, nt 1,659–3,791, GenBank: MT731686) and contains the *Efla* promoter of pSF-EF1Alpha (nt 238–1,442, Sigma-Aldrich, Merck, Darmstadt, Germany) controlling the expression of scFv-PD-1. The scFv-PD-1 gene encodes the murine immunoglobulin (Ig) kappa chain leader sequence of pSecTag2/A (nt 905–967, Invitrogen, Thermo Fisher Scientific, Waltham, MA) followed by the variable domain of the heavy chain (scFv 5C4 [Patent US 8008449 B2]), a polyGS-linker (GGGS₃), the variable domain of the light chain (scFv 5C4 [Patent US 8008449 B2]), a GS-linker, and a Myc-tag (EQKLISEEDL). The donor plasmid pGPS-SM2534 corresponds to pGPS-CMV/GFP-Kn-mFRT (same as for pGPS-SM2532) and contains the ampicillin-resistance gene of pCR3 (nt 3,568–4,599, Invitrogen, Thermo Fisher Scientific, Waltham, MA). It contains the scFv against EGFR of pSecTagA_scFv(hu225) (nt 85–807)⁶⁰ inserted between the sequence corresponding to amino acid 23 and 24 of HSV1 glycoprotein H (nt 46,315–46,383, nt 43,867–46,314, GenBank: JN555585), as described previously.³⁶

The plasmid pCAGGS-SM2667 corresponds to pCAGGS-*flpE-puro*⁶¹ (nt 1–2,401, nt 3,701–7,728, a gift of Rudolf Jaenisch [Addgene plasmid # 20733]) and contains the codon-optimized sequence of human EGFR (BioCat, Heidelberg, Germany).

Construction of the basic vector pB

To generate the pB vector for simplified genetic engineering of the HSV1 genome in *E. coli*, the genome of the most promising HSV1 isolate (acyclovir sensitive, most potent) was cloned as BAC. Therefore, essential bacterial genes together with some regulatory elements were inserted between *UL3* and *UL4* in a two-stage process in mammalian cells. First, a GFP encoding cassette and an additional polyadenylation signal derived from *UL21/UL22* were inserted to enhance the intergenic region. The NruI-ScaI fragment of pMA-SM2274 was co-transfected with isolated genomic viral DNA in a 1:5 ratio in Vero cells using Lipofectamine 3000 (Thermo Fisher Scientific, Waltham, MA). Green fluorescent infectious areas were isolated under the fluorescent microscope and four rounds of plaque purification were applied. Isolated genomic DNA of this fluorescently labeled HSV1 was co-transfected with linearized and dephosphorylated pBeloBAC11-SM2467 in 1:3 ratio in Vero cells using Lipofectamine 3000. After 1 day, Vero cells were overlaid with 1% LMP agarose/culture medium and further incubated. Two days post

Table 1. Sequences of oligonucleotides used

No	Name	Sequence	Use
1	pSF_1_fw	CCAACACACATACATGTTTCGATGGATAG	Gibson
2	pSF_1_rev	CCTTCTTCGCGTGCAGCAGATG	Gibson
3	pSF_2_fw	CATCTGCTGCACGCGGAAGAAGG	Gibson
4	pSF_2_rev	GGTAAGCGGCATGCTCGGAACAGG	Gibson
5	pSF_3_fw	CCTGTTCCGAGCATGCCGCTTACC	Gibson
6	pSF_3_rev	CGCTATCCATCGAACATGTATGTGTGTTGGTTTTTG	Gibson
7	pSF_1seq_fw	TCTGGCTCTATCGAATCTC	Sequencing
8	pSF_2seq_fw	GCGATTACCGTTGATGTTG	Sequencing
9	pSF_3seq_fw	CAGAATTGCGTCAGTCAAG	Sequencing
10	pUC_1_fw	ATTACGCCGGTACCCCAACCGACAGTCTGTGTA AAAAG	Gibson
11	pUC_1_rev	CACGTGTTGCGTGACGACAGCTTTGTAAAGAC	Gibson
12	pUC_2_b_fw	GTCGTCACGCAACACGTGTAGGGCGACAGGATTTG	Gibson
13	pUC_2neu_rev	GAATAACGACCCGAAGCTGCTCTCGCACTC	Gibson
14	pUC_4_fw	GCTTCGGGTCGTTATTTCAGTC	Gibson
15	pUC_4_rev	GCTTAACTATGCCGCATCAGAGC	Gibson
16	pUC_3neu_fw	CTGATGCCGCATAGTTAAGCCAGCC	Gibson
17	pUC_3_rev	TTGGGGTAACCGCGTAATCATGGTCATAGCTG	Gibson
18	pUC_1seq_fw	GCGCCCAATACGCAAAC	Sequencing
19	pUC_2seq_fw	AAACACGTCGAGCTGTTG	Sequencing
20	pUC_3seq_fw	ATTACACGCGATCTTCGG	Sequencing
21	ΔgalK_Cre_fw	GCGGCCGCTGCCAAGCTCCGAGCTCTCGAATCAAAGGAGGT ACCCACCATGCCAAGAAGAAGAGGAAGGTG	Construction basic vector
22	ΔlacZ_Cre_rev	GACTGTCCGTGTTGGGGTAACCAATGAGATTAGGGAGGG AAGAAAGTTGCTTAATAAATCTCGTATAGCATACATTAT	Construction basic vector
23	UL3-2_fw	cgcgattcattcgg	PCR control
24	UL4-7_rev	Gcgtatccgttgactc	PCR control
25	pBelo_seq_rev	GATTTCCGGCAGTTTCTACAC	PCR control
26	mFRT_Kan_Insertion_ UL10_11_F	TAACCCGACCGTGGTGTATGTCTGGTGTGTGGCGTCCGATC CCGTTACTATGTGGGCGGACAATAAAGTCTTAAACTGAA	Construction platform
27	UL11-AS_ mFRTKn_rev	TGTCGTTTTTAAAAAACCACAATCGCCGGGTTTGG GGGGAACGGTGATGTGGGCGGACAAAATAGTTGG	Construction platform
28	UL55_FRTKn_fw	AATAAAGAGCCGTAACCAACCAAAACCAGGCGTGGTGTG AGTTGTGGTGTGGGCGGACAATAAAGTCTTAAACTGAA	Construction platform
29	UL56-AS_FRTKn_rev	AGTATCACGGTCCATACTGGCCTGTCGCATTGTCTCTG AGGGCTTTGGGTTGTGGGCGGACAAAATAGTTGG	Construction platform
30	ICP6_Del_fw	CTCCCCGCTTCACCCTGGGTGGCGGCT GTTGTTCCTGTGCGGAGCACGAAGCCCA GCTGGTTAGGGATAACAGGGTAATCGATTT	Construction platform
31	ICP6_Del_rev	CCAGAGCCTGGGCCAGGATCACCAGCT GGGCTTCGTGCTCCGACAGGAACAACA GCCGCCAGTGTACAACCAATTAACC	Construction platform

transfection (dpt), 1% LMP agarose/culture medium with 300 μg/mL Blu-Gal was added. Three days post transfection, blue-labeled plaques were isolated and two rounds of plaque purification using LMP agarose/culture medium with Blu-Gal were performed. Hirt extract⁶² was used to transform electrocompetent *E. coli* DH10B (ElectroMAX DH10B, Thermo Fisher Scientific, Waltham, MA) un-

der 25 μg/mL chloramphenicol selection. Received clones were separated and controlled by isolation of BAC-DNA followed by restriction fragment-length polymorphism analysis. To control the integrity of the BAC-DNA, Vero cells were transfected and the reconstituted virus was analyzed regarding plaque size and growth kinetics, showing no difference to the virus isolate (data not shown).

To ensure the deletion of the bacterial genes after virus reconstitution, the lacZ selection cassette was exchanged for the Cre cassette fused to the Zeocin resistance cassette and a second *loxP* site using homologous recombination as described by Datsenko and Wanner.⁶³ To this end, *E. coli* DH10B carrying the vector and pKD46⁶³ were transformed with 400 ng of the linear fragment amplified by PCR using oligonucleotide no. 21/22 (Table 1) and pUC19-SM2479 as template. The removal of bacterial genes through Cre excision was investigated by PCR analysis using the isolated nucleic acids of reconstituted virus and oligonucleotide no. 23 together with no. 24 and oligonucleotide no. 23 together with 25 (Table 1). The received BAC-DNA was named pB vector (basic vector).

Construction of the platform vector pP

For insertion of the recombination sites FRT and mFRT into the intergenic regions of *UL10/UL11* and *UL55/UL56*,³⁰ respectively, a selection cassette was inserted according to the homologous recombination protocol described by Datsenko and Wanner.⁶³ The selection cassette that contains the kanamycin resistance gene flanked by FRT or mFRT, respectively, was amplified by PCR using pGPS-Kn-FRT/mFRT²⁵ as template and oligonucleotide no. 26/27 or oligonucleotide no. 28/29 (Table 1). Excision of the marker gene, the kanamycin resistance gene, was performed by transiently expressed Flpe recombinase as described previously,²⁷ except that pSC101-BAD-Flpe (Gene Bridges, Heidelberg, Germany) and therefore LB-agar plates containing 25 µg/mL chloramphenicol, 10 µg/µL tetracycline, and 0.4% (w/v) L-arabinose for selection and LB-agar plates containing 25 µg/µL chloramphenicol were used for further processing. The received BAC-DNA was named pP vector (platform vector).

Partial deletion of *UL39* and mutation of *UL37* were performed by *en passant* BAC mutagenesis.^{33,34} Thus, the platform vector was transformed into *E. coli* GS1783. Targeted mutation of *UL37* was done as described previously.³² To prevent transcription of *UL39* and to interfere neither with *UL38* nor *UL40*, a defined region of *UL39* (nt 498–1,385 of CDS) was deleted. Therefore, pEPkan-S2³⁴ and oligonucleotide no. 30/31 (Table 1) were used for PCR amplification prior to *en passant* mutagenesis. The received BAC-DNA was named pPNA (platform vector with attenuation and prevented neurotoxicity).

Functionalization of the platform vector - Insertion of transgenes

Insertion of transgenes into pPNA was performed using 100 ng of the donor plasmid (pGPS-SM2532, pGPS-SM2534) and 400 ng of the helper plasmid pGPS-Flpe (GenBank: MN687821) as described previously.²⁷

Viruses

To reconstitute (attenuated) virus, Vero cells at 50% confluency were transfected with isolated BAC-DNA using Lipofectamine 3000 according to manufacturer's protocol (Thermo Fisher Scientific, Waltham, MA). For further (attenuated) viral propagation, Vero cells (4 h after seeding) were infected and incubated until cytopathic effect (CPE) was observed. For (attenuated) virus titration via plaque assay, Vero cells at 90% confluency (4 h after seeding) were in-

fectured with 10-fold solutions of virus stock in triplicates. At 4 hpi, cells were overlaid with methylcellulose medium (7.5 g/L carboxymethylcellulose, 5% [v/v] fetal calf serum [FCS], 10% [v/v] MEM [10×], 1% [v/v] L-glutamine, 0.5% [v/v] non-essential amino acids, 1% [v/v] penicillin/streptomycin, 4.94% [v/v] sodium bicarbonate [7.5%]) and incubated for 3 (4) days followed by staining with crystal violet for 10 min at room temperature (RT) (2 g/L crystal violet, 11% [v/v] formaldehyde, 2% [v/v] ethanol, 20 g/L paraformaldehyde). For plaque purification⁶⁴ of (attenuated) virus, Vero cells at 80% confluency (4 h after seeding) were infected for 1 h (overnight) and then overlaid with LMP agarose/culture medium. To determine the growth kinetics of (attenuated) virus, Vero cells at 80% confluency (4 h after seeding) were infected with MOI 0.1 in triplicates. After 1 h, the inoculum was removed and infected cells were incubated in growth medium. The supernatants containing extracellular virus were collected at different time points and titrated via plaque assay. Plaque size was measured using Axiovision 4.8 (Zeiss, Oberkochen, Germany).

To evaluate transgene expression, cells were infected at MOI 0.5. At 20 hpi, the cells were lysed with RIPA buffer (0.1M Tris-HCl [pH 7.4], 0.75M NaCl, 5% [w/v] Triton X-100, 5% [w/v] sodium deoxycholate, 5% [w/v] SDS, protease inhibitor cocktail) on ice. The lysates were cleared by centrifugation (13,000 rpm, 4°C, 10 min) and further analyzed by SDS-PAGE followed by western blot using anti-Myc 9E10 antibodies (Santa Cruz Biotechnology, Dallas, TX) or via PD-1[Biotinylated]:PD-L1 Inhibitor Screening Assay (BPS Bioscience, San Diego, CA) using anti-PD-1 humanized antibodies (Pb3) (BioVision, Milpitas, CA) as control.

To follow the kinetic expression of the immunomodulating scFv-PD1, Vero cells were infected with the viruses PNA, PNAI, and PNAIT at MOI 0.1 or MOI 5. Cell lysates were prepared at varying times post infection and analyzed by western blot using anti-HSV-1 ICP0 antibody (Santa Cruz Biotechnology, Dallas, TX), anti-HSV1 + HSV2 ICP5/VP5 Major Capsid Protein antibody (3B6) (Abcam, Cambridge, UK), anti-HSV-1 and HSV-2 gB antibody (0B7)] (Abcam, Cambridge, UK), and anti-Myc 9E10 antibodies (Santa Cruz Biotechnology, Dallas, TX), as described above. As loading control, anti β-actin antibodies (Abcam, Cambridge, UK) were used.

To analyze the targeting of functionalized virus to EGFR-expressing cells, a cell-based assay was developed. J1.1-2, J-EGFR and J-EGFR cells pre-incubated with anti-EGFR chimeric antibodies (Ce3) (BioVision, Milpitas, CA) (30 min, 4°C) were infected with virus (MOI 5). At 20 hpi, cells were harvested and samples were analyzed by western blot using anti-gB vc-14 antibodies (Santa Cruz Biotechnology, Dallas, TX), as described above.

To determine killing curves of lung carcinoma cell lines after infection, the cell viability was measured using neutral red uptake assay. To this end, 6×10^3 A549 and 3×10^3 HCC827 cells were seeded in a 96-well plate and infected 4 h later (MOI 0.5). After 1 h, the inoculum was removed and cells were incubated in growth medium.

Neutral red uptake assay was performed at different time points as described previously.⁶⁵

Virus killing assay on 2D respective 3D patient-derived models and non-cancer cells

A previously established and characterized 2D patient-derived cell line from an NSCLC primary tumor was seeded in a μ Clear 384-well plate (1,500/well) in PCCM. The PCCM consists of advanced DMEM/F12, 5% SAM-FCS (PAN-Biotech, Aidenbach, Germany), 1% Glutamax, 1% penicillin/streptomycin, 1 μ g/ μ L insulin (PAN-Biotech, Aidenbach, Germany), 10 ng/mL epidermal growth factor (EGF) (Thermo Fisher, Germany), 50 μ M hydrocortisone (Sigma-Aldrich, Merck, Darmstadt, Germany), and 10 μ M Y27632 (Selleckchem, Munich, Germany). After 3 h, the PNA or PNAIT virus dilutions (MOI 0.01–1) were added at a final volume of 40 μ L of PCCM. At 4 dpi, the plate was removed from the incubator, equilibrated for 30 min at RT, and 40 μ L of ATPlite were added in every well before mixing for 2 min at 1,200rpm. The luminescence was measured using the PerkinElmer's EnVision Multimode Plate Reader. The percentage of surviving cells is normalized on the untreated control, five replicates were made for each MOI value, and two independent experiments were performed. The toxicity on non-cancer cells was tested *in vitro* on T cells. Therefore, peripheral blood mononuclear cells (PBMCs) were isolated and propagated by stimulation with 2 μ g/mL CD3 (BioLegend, Amsterdam, the Netherlands), 2 μ g/mL CD28 (BioLegend, Amsterdam, the Netherlands), and 150 U/mL IL-2 (BioLegend, Amsterdam the Netherlands). The virus killing assay on T cells was performed exactly in the same way as the 2D model; only the medium differed. The T cell medium consists of a base medium (RPMI 1640, 1% Glutamax, 1% penicillin/streptomycin, 1% HEPES, 5 μ M 2-mercaptoethanol) with 10% human AB-serum (Valley Biomedical Products & Services, Winchester, VA) mixed 1:1 with AIM-V medium (Thermo Fisher Scientific, Waltham, MA).

Similar to the 2D assay, established and characterized patient-derived organoids (PDOs) (3D) were seeded in a μ Clear 384-well plate (500 organoids/well) in organoids medium⁶⁶ without Matrigel for the 3D assay. After settling of the PDOs, PNA or PNAIT virus dilutions (MOI 0.1–10) were added at a final volume of 40 μ L of organoids medium. At 3 dpi, the plate was equilibrated for 30 min at RT and 40 μ L of CellTiter-Glo (CTG, Promega Corporation, Fitchburg, MA) were added in every well before shaking for 5 min at 800 rpm and incubation at RT for 25 min. The luminescence was measured using the PerkinElmer's EnVision Multimode Plate Reader. The percentage of surviving organoids was normalized on the untreated control, five replicates were performed for each MOI value, and the experiment was done three times independently.

Matrix preparation for 3D tissue model

Chemical decellularization of jejunal segments was performed as previously described.^{67–69} The intestinal segments were explanted, rinsed with PBS, and chemically decellularized with a sodium deoxycholate monohydrate solution; the former vascular tree was manually

removed prior to gamma sterilization. Finally, tumor models were prepared as published before.¹⁹

Determination of cell number on static 3D tumor model

After removing the unseeded parts of the SISmuc, cells were separated by trypsinization followed by scraping with a cell scraper. After filtering the cell suspension with a filter (40 μ m), cells were counted with a Neubauer chamber.

Treatment of a static 3D model with virus

According to the mean cell numbers determined on the SISmuc, a suspension of virus stock was added at day 11 to the medium in the inner compartment of a cell crown to reach the respective MOI (medium volume in the inner compartment of the cell crown, 1 mL; medium volume in the outer compartment of the cell crown, 1.5 mL).

Humanization of NSG mice

The 24- to 48-h-old NOD.Cg-Prdc^{scid}IL2r γ ^{tm1Wjl}/SzJ (NSG, Jackson Laboratory, Bar Harbor, ME) were irradiated with 1 Gy using Small Animal Radiation Research Platform (SARRP, XStrahl, GA). At 3–5 h after irradiation, intrahepatic injection of 2–4 \times 10⁵ human CD34⁺ hematopoietic stem cells per mouse in RPMI-1640 medium containing 10% FCS was performed. After 12 weeks, blood was analyzed to determine the cellular composition by flow cytometry. NSG mice were considered to be humanized when 20% or more of all CD45⁺ cells in peripheral blood were of human origin.

NSCLC tumor model in NSG mice and oncolytic virotherapy

Solid tumor experiments were performed using immunodeficient NOD.Cg-Prkdc^{scid} Il2rg^{tm1Wjl}/SzJ mice (NSG, Jackson Laboratory, Bar Harbor, ME). All experiments were performed in accordance with EU Directive 2010/63/EU for animal experiments and approved by local authorities. Tumor induction was performed under isoflurane anesthesia by injecting 2 \times 10⁵ reporter cells (A549^{Luc} or HCC827^{Luc}) in 100 μ L of PBS subcutaneously in one mouse flank. Mice were clinically assessed two or three times weekly and the tumor volume was determined and scored using the following scoring system: 0 (no tumor growth or tumor volume <500mm³), 5 (tumor volume \geq 0.5cm³), 10 (tumor volume \geq 1 cm³), or 20 (tumor volume \geq 1.5cm³, corresponds to human endpoint). The tumor volume was calculated by measuring width and length of the palpable tumor (volume = (length \times width \times width)/2). In addition, the clinical score was obtained for following abnormalities: 0 (no weight loss or gain), 1 (<5% weight loss), 5 (\geq 5% weight loss), 10 (\geq 10% weight loss), or 20 (\geq 20% weight loss, corresponds to human endpoint); 0, 1, 5, or 10 points for fur defects; 10 points for hunched position, lethargy, or coordination disorders; 20 points for respiratory difficulties, visible tumor necrosis, paralysis, morbidity, or death (corresponds to human endpoint, respectively). After solid tumor formation of \sim 100 mm³, experimental groups were formed in order to obtain a homogeneous distribution of tumor volumes in each group. Virotherapy was performed by intratumoral injection of 30 μ L of virus in PBS. Bioluminescence imaging (BLI) was used to monitor tumor growth, since an increase in tumor cell number correlates with bioluminescence.

For this purpose, mice were anesthetized with isoflurane and 150 mg/kg D-luciferin (PerkinElmer, Waltham, MA) was injected intraperitoneally. After incubation for 20 min, bioluminescence measurement was performed using IVIS spectrum (Xenogen, PerkinElmer, Waltham, MA). Bioluminescence signals were evaluated using Living Image 3.2 software (PerkinElmer, Waltham, MA) as photons per area. Statistical analysis was performed by Mann-Whitney U test in comparison to non-treated control.

Real-time qPCR

Viral DNA was isolated from tumor and brain using gentleMACS Octo Dissociator (Miltenyi Biotec, Bergisch Gladbach, Germany) for tissue homogenization and QIAamp MinElute Virus Spin Kit (Qiagen, Hilden, Germany) for DNA isolation. Quantitative detection of HSV1-DNA was performed using LightCycler 480 (Roche Holding, Basel, Switzerland), 5 µL of viral DNA by real-time PCR protocol as described,^{70,71} and LightCycler FastStart DNA MasterPlus Hybridization Probes Kit (Roche Holding AG, Basel, Switzerland). Absolute DNA quantification was performed using standard curve and DNA dilutions of 30 to 3×10^6 HSV1 copies. Limit of detection (LOD) was defined as to 30 DNA copies.

Immunohistochemical staining

The 3D tumor models were fixed in a 4% PFA solution for 2 h, embedded in paraffin, and cut with a sliding microtome at 3–5 µm. Hematoxylin and eosin (H&E) staining (Morphisto, Offenbach am Main, Germany) was performed according to the manufacturer's protocol. The following primary antibodies were used: rabbit anti-vimentin (Abcam, Cambridge, UK), mouse anti-HSV1 VP21/VP22a (Bio-Rad Laboratories, Hercules, CA). Primary antibodies were diluted 1:100 in antibody diluent (DCS Innovative Diagnostik-Systeme, Hamburg, Germany) and incubated overnight at 4°C. Secondary antibodies (donkey anti-mouse IgG [Thermo Fisher Scientific, Waltham, MA] conjugated to Alexa 647 or donkey anti-rabbit IgG [Thermo Fisher Scientific, Waltham, MA] conjugated to Alexa 555) were diluted 1:400 in antibody diluent and incubated for 1 h at RT. Cell nuclei were counterstained using 4',6-diamidino-2-phenylindole (DAPI) within the embedding medium Fluoromount-G (Thermo Fisher Scientific, Waltham, MA). Images were taken using a digital microscope (BZ-9000, Keyence, Japan).

For immunohistological detection of HSV1 and apoptosis in tumor tissue, tumor tissue samples of mice were fixed in 4% buffered paraformaldehyde solution (PFA, Sigma-Aldrich, Merck, Darmstadt, Germany) for 24 h after explantation. Specimens were embedded in paraffin and transferred to slides as 4- to 6-µm sections. Immunostaining was performed after antigen demasking (30 min in preheated 10 mM citrate buffer) either for HSV1 or TUNEL staining (detection of apoptosis-induced fragmented DNA). After blocking non-specific binding using 5% goat serum (Abcam, Cambridge, UK) and 0.3% Triton X-(Sigma-Aldrich, Merck, Darmstadt, Germany) in PBS for 1 h, HSV staining was performed using primary antibody mouse anti-HSV1 + HSV2 ICP5 (1:400, Abcam, Cambridge, UK) overnight at 4°C and secondary antibody goat anti-mouse IgG

Alexa Fluor 647 (1:400, Thermo Fisher Scientific, Waltham, MA) for 2 h in blocking buffer. TUNEL staining was performed using the In Situ Cell Death Detection Kit (Roche Holding, Basel, Switzerland). Nuclei were stained by incubating with 2.5 µg/mL DAPI (Sigma-Aldrich, Merck, Darmstadt, Germany) solution for 10 min. Specimens were coverslipped with Dako Fluorescence Mounting Medium (Agilent Technologies, Santa Clara, CA) and evaluation was performed by Eclipse Ti fluorescence microscope (Nikon, Tokio, Japan).

General methods

Isolation of BAC-DNA was performed using standard phenol-chloroform isolation.

Isolation of viral nucleic acids was done using High Pure Viral Nucleic Acid Kit (Roche Holding, Basel, Switzerland). Genomic viral DNA from capsids was isolated as described elsewhere.⁷² Preparation of electrocompetent *E. coli* DH10B or *E. coli* GS1783 (genotype: W3110 ΔlacU169 gal490 λN:lacZ Δ(N-int) cI857 Δ(cro-bioA)) and transformation was done as described previously.^{27,33,34,73,74} After BAC mutagenesis, *E. coli* colonies were separated and controlled by isolation of BAC-DNA followed by analysis of restriction fragment-length polymorphism, control of PCR fragment, and local sequencing.

DATA AND CODE AVAILABILITY

All data are available in the main text.

SUPPLEMENTAL INFORMATION

Supplemental information can be found online at <https://doi.org/10.1016/j.omton.2024.200784>.

ACKNOWLEDGMENTS

We would like to acknowledge Gabriella Campadelli-Fiume for kindly providing the J1.1-2 cells. We thank Isabell Schulz, Joe Fischer, Eric Possardt, Anne-Kathrin Donner, Sebastian Greiser, Sandra Weller, Carolin Kroll, Laura Glück, Victor Carvalho Urbietta, Jana Hessel, Jessica Marsal, Heide Häfner, Lisa Wirth, and Dagmar Halbritter for excellent assistance and Max Guthardt and Franziska Lange for the generation of humanized NSG mice. We would like to acknowledge the generous funding for the MAVO TheraVision project provided by the Fraunhofer Society, Munich, Germany.

AUTHOR CONTRIBUTIONS

Conceptualization, G.D., T.G., C.W., and S.M.B.; methodology, Z.R.; investigation, C.F., C.B., K.E., G.V., N.U., S.N., M.P., and F.B.; writing – original draft, C.F., N.U., G.D., C.B., C.W., T.G., and S.M.B.; writing – reviewing & editing, C.F., N.U., G.D., T.G., C.W., Z.R., and S.M.B.; supervision and funding acquisition, G.D., T.G., C.W., and S.M.B.

DECLARATION OF INTERESTS

A patent is pending filed by Funk and Bailer entitled "platform vector based on herpes simplex virus 1 (HSV1) for the modular insertion of transgenes for use in oncolytic virus therapy."

REFERENCES

- International Agency for Research on Cancer (2022). Estimated number of deaths in 2020, World, both sexes, all ages. https://gco.iarc.fr/today/online-analysis-pie?v=2020&mode=cancer&mode_population=continents&population=900&populations=900&key=total&sex=0&cancer=39&type=1&statistic=5&prevalence=0&population_group=0&ages_group%5B%5D=0&ages_group%5B%5D=17&nb_items=7&group_cancer=1&include_nmsc=1&include_nmsc_other=1&half_pie=0&donut=0.
- Russell, S.J., Peng, K.-W., and Bell, J.C. (2012). Oncolytic virotherapy. *Nat. Biotechnol.* 30, 658–670. <https://doi.org/10.1038/nbt.2287>.
- Sharma, P., and Allison, J.P. (2015). The future of immune checkpoint therapy. *Science* 348, 56–61. <https://doi.org/10.1126/science.aaa8172>.
- Kyi, C., and Postow, M.A. (2016). Immune checkpoint inhibitor combinations in solid tumors: opportunities and challenges. *Immunotherapy* 8, 821–837. <https://doi.org/10.2217/imt-2016-0002>.
- Brahmer, J.R., and Pardoll, D.M. (2013). Immune checkpoint inhibitors: making immunotherapy a reality for the treatment of lung cancer. *Cancer Immunol. Res.* 1, 85–91. <https://doi.org/10.1158/2326-6066.CIR-13-0078>.
- Topalian, S.L., Hodi, F.S., Brahmer, J.R., Gettinger, S.N., Smith, D.C., McDermott, D.F., Powderly, J.D., Carvajal, R.D., Sosman, J.A., Atkins, M.B., et al. (2012). Safety, activity, and immune correlates of anti-PD-1 antibody in cancer. *N. Engl. J. Med.* 366, 2443–2454. <https://doi.org/10.1056/NEJMoa1200690>.
- Kaufman, H.L., Kohlhapp, F.J., and Zloza, A. (2015). Oncolytic viruses: a new class of immunotherapy drugs. *Nat. Rev. Drug Discov.* 14, 642–662. <https://doi.org/10.1038/nrd4663>.
- Achard, C., Surendran, A., Wedge, M.-E., Ungerechts, G., Bell, J., and Ilkow, C.S. (2018). Lighting a Fire in the Tumor Microenvironment Using Oncolytic Immunotherapy. *EBioMedicine* 31, 17–24. <https://doi.org/10.1016/j.ebiom.2018.04.020>.
- Liu, B.L., Robinson, M., Han, Z.-Q., Branstor, R.H., English, C., Reay, P., McGrath, Y., Thomas, S.K., Thornton, M., Bullock, P., et al. (2003). ICP34.5 deleted herpes simplex virus with enhanced oncolytic, immune stimulating, and anti-tumour properties. *Gene Ther.* 10, 292–303. <https://doi.org/10.1038/sj.gt.3301885>.
- Chen, C.-Y., Hutzen, B., Wedekind, M.F., and Cripe, T.P. (2018). Oncolytic virus and PD-1/PD-L1 blockade combination therapy. *Oncolytic Virotherapy* 7, 65–77. <https://doi.org/10.2147/OV.S145532>.
- Sasso, E., D'Alise, A.M., Zambrano, N., Scarselli, E., Folgori, A., and Nicosia, A. (2020). New viral vectors for infectious diseases and cancer. *Semin. Immunol.* 50, 101430. <https://doi.org/10.1016/j.smim.2020.101430>.
- Nettelbeck, D.M., Leber, M.F., Altomonte, J., Angelova, A., Beil, J., Berchtold, S., Delic, M., Eberle, J., Ehrhardt, A., Engeland, C.E., et al. (2021). Virotherapy in Germany—Recent Activities in Virus Engineering, Preclinical Development, and Clinical Studies. *Viruses* 13, 1420. <https://doi.org/10.3390/v13081420>.
- Menotti, L., and Avitabile, E. (2020). Herpes Simplex Virus Oncolytic Immunovirotherapy: The Blossoming Branch of Multimodal Therapy. *Int. J. Mol. Sci.* 21, 8310. <https://doi.org/10.3390/ijms21218310>.
- Kumar, A., Taghi Khani, A., Sanchez Ortiz, A., and Swaminathan, S. (2022). A Double-Edged Sword in Cancer Immunotherapy. *Front. Immunol.* 13, 901277. <https://doi.org/10.3389/fimmu.2022.901277>.
- Vlachogiannis, G., Hedayat, S., Vatsiou, A., Jamin, Y., Fernández-Mateos, J., Khan, K., Lampis, A., Eason, K., Huntingford, I., Burke, R., et al. (2018). Patient-derived organoids model treatment response of metastatic gastrointestinal cancers. *Science* 359, 920–926. <https://doi.org/10.1126/science.aao2774>.
- Lee, J.-K., Liu, Z., Sa, J.K., Shin, S., Wang, J., Bordyuh, M., Cho, H.J., Elliott, O., Chu, T., Choi, S.W., et al. (2018). Pharmacogenomic landscape of patient-derived tumor cells informs precision oncology therapy. *Nat. Genet.* 50, 1399–1411. <https://doi.org/10.1038/s41588-018-0209-6>.
- Schnalzger, T.E., Groot, M.H. de, Zhang, C., Mosa, M.H., Michels, B.E., Röder, J., Darvishi, T., Wels, W.S., and Farin, H.F. (2019). 3D model for CAR-mediated cytotoxicity using patient-derived colorectal cancer organoids. *EMBO J.* 38. <https://doi.org/10.15252/embj.2018100928>.
- Dijkstra, K.K., Cattaneo, C.M., Weeber, F., Chalabi, M., van de Haar, J., Fanchi, L.F., Slagter, M., van der Velden, D.L., Kaing, S., Kelderman, S., et al. (2018). Generation of Tumor-Reactive T Cells by Co-culture of Peripheral Blood Lymphocytes and Tumor Organoids. *Cell* 174, 1586–1598.e12. <https://doi.org/10.1016/j.cell.2018.07.009>.
- Kühnemundt, J., Leifeld, H., Scherg, F., Schmitt, M., Nelke, L.C., Schmitt, T., Baur, F., Göttlich, C., Fuchs, M., Kunz, M., et al. (2020). Modular micro-physiological human tumor/tissue models based on decellularized tissue for improved preclinical testing. *ALTEX* 38, 289–306. <https://doi.org/10.14573/altex.2008141>.
- Wojton, J., and Kaur, B. (2010). Impact of tumor microenvironment on oncolytic viral therapy. *Cytokine Growth Factor Rev.* 21, 127–134. <https://doi.org/10.1016/j.cytogfr.2010.02.014>.
- Chiu, M., Armstrong, E.J.L., Jennings, V., Foo, S., Crespo-Rodriguez, E., Bozhanova, G., Patin, E.C., McLaughlin, M., Mansfield, D., Baker, G., et al. (2020). Combination therapy with oncolytic viruses and immune checkpoint inhibitors. *Expert Opin. Biol. Ther.* 20, 635–652. <https://doi.org/10.1080/14712598.2020.1729351>.
- Shultz, L.D., Brehm, M.A., Garcia-Martinez, J.V., and Greiner, D.L. (2012). Humanized mice for immune system investigation: progress, promise and challenges. *Nat. Rev. Immunol.* 12, 786–798. <https://doi.org/10.1038/nri3311>.
- Wang, M., Yao, L.-C., Cheng, M., Cai, D., Martinek, J., Pan, C.-X., Shi, W., Ma, A.H., De Vere White, R.W., Airhart, S., et al. (2018). Humanized mice in studying efficacy and mechanisms of PD-1-targeted cancer immunotherapy. *Faseb. J.* 32, 1537–1549. <https://doi.org/10.1096/fj.201700740R>.
- Rosato, R.R., Dávila-González, D., Choi, D.S., Qian, W., Chen, W., Kozielski, A.J., Wong, H., Dave, B., and Chang, J.C. (2018). Evaluation of anti-PD-1-based therapy against triple-negative breast cancer patient-derived xenograft tumors engrafted in humanized mouse models. *Breast Cancer Res.* 20, 108. <https://doi.org/10.1186/s13058-018-1037-4>.
- Ruzsics, Z., Lemnitzer, F., and Thirion, C. (2014). Engineering adenovirus genome by bacterial artificial chromosome (BAC) technology. *Methods Mol. Biol.* 1089, 143–158. https://doi.org/10.1007/978-1-62703-679-5_11.
- Bailer, S.M., Funk, C., Riedl, A., and Ruzsics, Z. (2017). Herpesviral vectors and their application in oncolytic therapy, vaccination, and gene transfer. *Virus Gene.* 53, 741–748. <https://doi.org/10.1007/s11262-017-1482-7>.
- Riedl, A., Gruber, S., and Ruzsics, Z. (2020). Novel conditional plasmids regulated by chemical switches provide versatile tools for genetic engineering in *Escherichia coli*. *Plasmid* 111, 102531. <https://doi.org/10.1016/j.plasmid.2020.102531>.
- Baines, J.D., and Roizman, B. (1991). The open reading frames UL3, UL4, UL10, and UL16 are dispensable for the replication of herpes simplex virus 1 in cell culture. *J. Virol.* 65, 938–944. <https://doi.org/10.1128/JVI.65.2.938-944.1991>.
- Schlake, T., and Bode, J. (1994). Use of mutated FLP recognition target (FRT) sites for the exchange of expression cassettes at defined chromosomal loci. *Biochemistry* 33, 12746–12751. <https://doi.org/10.1021/bi00209a003>.
- Morimoto, T., Arii, J., Akashi, H., and Kawaguchi, Y. (2009). Identification of multiple sites suitable for insertion of foreign genes in herpes simplex virus genomes. *Microbiol. Immunol.* 53, 155–161. <https://doi.org/10.1111/j.1348-0421.2008.00104.x>.
- Peters, C., and Rabkin, S.D. (2015). Designing Herpes Viruses as Oncolytics. *Mol. Ther. Oncolytics* 2, 15010. <https://doi.org/10.1038/mto.2015.10>.
- Richards, A.L., Sollars, P.J., Pitts, J.D., Stults, A.M., Heldwein, E.E., Pickard, G.E., and Smith, G.A. (2017). The pUL37 tegument protein guides alpha-herpesvirus retrograde axonal transport to promote neuroinvasion. *PLoS Pathog.* 13, e1006741. <https://doi.org/10.1371/journal.ppat.1006741>.
- Tischer, B.K., Smith, G.A., and Osterrieder, N. (2010). En passant mutagenesis: a two step markerless red recombination system. *Methods Mol. Biol.* 634, 421–430. https://doi.org/10.1007/978-1-60761-652-8_30.
- Tischer, B.K., von Einem, J., Kaufer, B., and Osterrieder, N. (2006). Two-step red-mediated recombination for versatile high-efficiency markerless DNA manipulation in *Escherichia coli*. *Biotechniques* 40, 191–197. <https://doi.org/10.2144/000112096>.
- Connor, R.I., Chen, B.K., Choe, S., and Landau, N.R. (1995). Vpr is required for efficient replication of human immunodeficiency virus type-1 in mononuclear phagocytes. *Virology* 206, 935–944. <https://doi.org/10.1006/viro.1995.1016>.
- Gatta, V., Petrovic, B., and Campadelli-Fiume, G. (2015). The Engineering of a Novel Ligand in gH Confers to HSV an Expanded Tropism Independent of gD Activation by Its Receptors. *PLoS Pathog.* 11, e1004907. <https://doi.org/10.1371/journal.ppat.1004907>.

37. Cocchi, F., Menotti, L., Mirandola, P., Lopez, M., and Campadelli-Fiume, G. (1998). The ectodomain of a novel member of the immunoglobulin subfamily related to the poliovirus receptor has the attributes of a bona fide receptor for herpes simplex virus types 1 and 2 in human cells. *J. Virol.* 72, 9992–10002. <https://doi.org/10.1128/JVI.72.12.9992-10002.1998>.
38. Riedl, A., Fischer, J., Burgert, H.-G., and Ruzsics, Z. (2022). Rescue of Recombinant Adenoviruses by CRISPR/Cas-Mediated in vivo Terminal Resolution. *Front. Microbiol.* 13, 854690. <https://doi.org/10.3389/fmicb.2022.854690>.
39. Broach, J.R., Guarascio, V.R., and Jayaram, M. (1982). Recombination within the yeast plasmid 2mu circle is site-specific. *Cell* 29, 227–234. [https://doi.org/10.1016/0092-8674\(82\)90107-6](https://doi.org/10.1016/0092-8674(82)90107-6).
40. Broach, J.R., and Hicks, J.B. (1980). Replication and recombination functions associated with the yeast plasmid, 2 mu circle. *Cell* 21, 501–508. [https://doi.org/10.1016/0092-8674\(80\)90487-0](https://doi.org/10.1016/0092-8674(80)90487-0).
41. Martin, N.T., and Bell, J.C. (2018). Oncolytic Virus Combination Therapy: Killing One Bird with Two Stones. *Mol. Ther.* 26, 1414–1422. <https://doi.org/10.1016/j.ymthe.2018.04.001>.
42. Speranza, M.-C., Kasai, K., and Lawler, S.E. (2016). Preclinical Mouse Models for Analysis of the Therapeutic Potential of Engineered Oncolytic Herpes Viruses. *ILAR J.* 57, 63–72. <https://doi.org/10.1093/ilar/ilw002>.
43. Chen, C.-Y., Wang, P.-Y., Hutzen, B., Sprague, L., Swain, H.M., Love, J.K., Stanek, J.R., Boon, L., Conner, J., and Cripe, T.P. (2017). Cooperation of Oncolytic Herpes Virotherapy and PD-1 Blockade in Murine Rhabdomyosarcoma Models. *Sci. Rep.* 7, 2396. <https://doi.org/10.1038/s41598-017-02503-8>.
44. Raimondi, G., Mato-Berciano, A., Pascual-Sabater, S., Rovira-Rigau, M., Cuatrecasas, M., Fondevila, C., Sánchez-Cabús, S., Begthel, H., Boj, S.F., Clevers, H., and Fillat, C. (2020). Patient-derived pancreatic tumour organoids identify therapeutic responses to oncolytic adenoviruses. *EBioMedicine* 56, 102786. <https://doi.org/10.1016/j.ebiom.2020.102786>.
45. Lübtow, M.M., Nelke, L.C., Seifert, J., Kühnemundt, J., Sahay, G., Dandekar, G., Nietzer, S.L., and Luxenhofer, R. (2019). Drug induced micellization into ultra-high capacity and stable curcumin nanoformulations: Physico-chemical characterization and evaluation in 2D and 3D in vitro models. *J. Contr. Release* 303, 162–180. <https://doi.org/10.1016/j.jconrel.2019.04.014>.
46. Nietzer, S., Baur, F., Sieber, S., Hansmann, J., Schwarz, T., Stoffer, C., Häfner, H., Gasser, M., Waaga-Gasser, A.M., Walles, H., and Dandekar, G. (2016). Mimicking Metastases Including Tumor Stroma: A New Technique to Generate a Three-Dimensional Colorectal Cancer Model Based on a Biological Decellularized Intestinal Scaffold. *Tissue Eng. C Methods* 22 (7), 621–635. <https://doi.org/10.1089/ten.TEC.2015.0557>.
47. Wallstabe, L., Göttlich, C., Nelke, L.C., Kühnemundt, J., Schwarz, T., Nerretter, T., Einsele, H., Walles, H., Dandekar, G., Nietzer, S.L., and Hudecek, M. (2019). ROR1-CAR T cells are effective against lung and breast cancer in advanced microphysiologic 3D tumor models. *JCI Insight* 4, e126345. <https://doi.org/10.1172/jci.insight.126345>.
48. Stüber, T., Monjezi, R., Wallstabe, L., Kühnemundt, J., Nietzer, S.L., Dandekar, G., Wöckel, A., Einsele, H., Wischhusen, J., and Hudecek, M. (2020). Inhibition of TGF- β -receptor signaling augments the antitumor function of ROR1-specific CAR T-cells against triple-negative breast cancer. *J. Immunother. Cancer* 8, e000676. <https://doi.org/10.1136/jitc-2020-000676>.
49. Smith, G.A., and Enquist, L.W. (2000). A self-recombining bacterial artificial chromosome and its application for analysis of herpesvirus pathogenesis. *Proc. Natl. Acad. Sci. USA* 97, 4873–4878. <https://doi.org/10.1073/pnas.080502497>.
50. Smiley, M.L., Hoxie, J.A., and Friedman, H.M. (1985). Herpes simplex virus type 1 infection of endothelial, epithelial, and fibroblast cells induces a receptor for C3b. *J. Immunol.* 134, 2673–2678.
51. Martinez-Quintanilla, J., Seah, I., Chua, M., and Shah, K. (2019). Oncolytic viruses: overcoming translational challenges. *J. Clin. Invest.* 129, 1407–1418. <https://doi.org/10.1172/JCI122287>.
52. Sitta, J., Claudio, P.P., and Howard, C.M. (2022). Virus-Based Immuno-Oncology Models. *Biomedicines* 10, 1441. <https://doi.org/10.3390/biomedicines10061441>.
53. Runge, A., Mayr, M., Schwaiger, T., Sprung, S., Chetta, P., Gottfried, T., Dudas, J., Greier, M.C., Glatz, M.C., Haybaeck, J., et al. (2022). Patient-derived head and neck tumor slice cultures: a versatile tool to study oncolytic virus action. *Sci. Rep.* 12, 15334. <https://doi.org/10.1038/s41598-022-19555-0>.
54. Twumasi-Boateng, K., Pettigrew, J.L., Kwok, Y.Y.E., Bell, J.C., and Nelson, B.H. (2018). Oncolytic viruses as engineering platforms for combination immunotherapy. *Nat. Rev. Cancer* 18, 419–432. <https://doi.org/10.1038/s41568-018-0009-4>.
55. Larson, C., Oronsky, B., Scicinski, J., Fanger, G.R., Stirn, M., Oronsky, A., and Reid, T.R. (2015). Going viral: a review of replication-selective oncolytic adenoviruses. *Oncotarget* 6, 19976–19989. <https://doi.org/10.18632/oncotarget.5116>.
56. Macedo, N., Miller, D.M., Haq, R., and Kaufman, H.L. (2020). Clinical landscape of oncolytic virus research in 2020. *J. Immunother. Cancer* 8, e001486. <https://doi.org/10.1136/jitc-2020-001486>.
57. Kawaguchi, Y., van Sant, C., and Roizman, B. (1997). Herpes simplex virus 1 alpha regulatory protein ICP0 interacts with and stabilizes the cell cycle regulator cyclin D3. *J. Virol.* 71, 7328–7336.
58. Tanaka, M., Kagawa, H., Yamanashi, Y., Sata, T., and Kawaguchi, Y. (2003). Construction of an excisable bacterial artificial chromosome containing a full-length infectious clone of herpes simplex virus type 1: viruses reconstituted from the clone exhibit wild-type properties in vitro and in vivo. *J. Virol.* 77, 1382–1391. <https://doi.org/10.1128/jvi.77.2.1382-1391.2003>.
59. Bubeck, A., Wagner, M., Ruzsics, Z., Lötzerich, M., Iglesias, M., Singh, I.R., and Koszinowski, U.H. (2004). Comprehensive mutational analysis of a herpesvirus gene in the viral genome context reveals a region essential for virus replication. *J. Virol.* 78, 8026–8035. <https://doi.org/10.1128/JVI.78.15.8026-8035.2004>.
60. Seifert, O., Plappert, A., Heidel, N., Fellermeier, S., Messerschmidt, S.K.E., Richter, F., and Kontermann, R.E. (2012). The IgM CH2 domain as covalently linked homodimerization module for the generation of fusion proteins with dual specificity. *Protein Eng. Des. Sel.* 25, 603–612. <https://doi.org/10.1093/protein/gzso59>.
61. Beard, C., Hochedlinger, K., Plath, K., Wutz, A., and Jaenisch, R. (2006). Efficient method to generate single-copy transgenic mice by site-specific integration in embryonic stem cells. *Genesis* 44, 23–28. <https://doi.org/10.1002/gene.20180>.
62. Hirt, B. (1967). Selective extraction of polyoma DNA from infected mouse cell cultures. *J. Mol. Biol.* 26, 365–369. [https://doi.org/10.1016/0022-2836\(67\)90307-5](https://doi.org/10.1016/0022-2836(67)90307-5).
63. Datsenko, K.A., and Wanner, B.L. (2000). One-step inactivation of chromosomal genes in *Escherichia coli* K-12 using PCR products. *Proc. Natl. Acad. Sci. USA* 97, 6640–6645. <https://doi.org/10.1073/pnas.120163297>.
64. Nagel, C.-H., Pohlmann, A., and Sodeik, B. (2014). Construction and characterization of bacterial artificial chromosomes (BACs) containing herpes simplex virus full-length genomes. *Methods Mol. Biol.* 1144, 43–62. https://doi.org/10.1007/978-1-4939-0428-0_4.
65. Repetto, G., Del Peso, A., and Zurita, J.L. (2008). Neutral red uptake assay for the estimation of cell viability/cytotoxicity. *Nat. Protoc.* 3, 1125–1131. <https://doi.org/10.1038/nprot.2008.75>.
66. Dekkers, J.F., van Vliet, E.J., Sachs, N., Rosenbluth, J.M., Kopper, O., Rebel, H.G., Wehrens, E.J., Piani, C., Visvader, J.E., Verissimo, C.S., et al. (2021). Long-term culture, genetic manipulation and xenotransplantation of human normal and breast cancer organoids. *Nat. Protoc.* 16, 1936–1965. <https://doi.org/10.1038/s41596-020-00474-1>.
67. Jannasch, M., Groeber, F., Brattig, N.W., Unger, C., Walles, H., and Hansmann, J. (2015). Development and application of three-dimensional skin equivalents for the investigation of percutaneous worm invasion. *Exp. Parasitol.* 150, 22–30. <https://doi.org/10.1016/j.exppara.2015.01.005>.
68. Linke, K., Schanz, J., Hansmann, J., Walles, T., Brunner, H., and Mertsching, H. (2007). Engineered liver-like tissue on a capillarized matrix for applied research. *Tissue Eng.* 13, 2699–2707. <https://doi.org/10.1089/ten.2006.0388>.
69. Schanz, J., Pusch, J., Hansmann, J., and Walles, H. (2010). Vascularised human tissue models: a new approach for the refinement of biomedical research. *J. Biotechnol.* 148, 56–63. <https://doi.org/10.1016/j.jbiotec.2010.03.015>.
70. Burrows, J., Nitsche, A., Bayly, B., Walker, E., Higgins, G., and Kok, T. (2002). Detection and subtyping of Herpes simplex virus in clinical samples by LightCycler PCR, enzyme immunoassay and cell culture. *BMC Microbiol.* 2, 12. <https://doi.org/10.1186/1471-2180-2-12>.

71. Stang, A., Korn, K., Wildner, O., and Uberla, K. (2005). Characterization of virus isolates by particle-associated nucleic acid PCR. *J. Clin. Microbiol.* 43, 716–720. <https://doi.org/10.1128/JCM.43.2.716-720.2005>.
72. Maclean, A.R. (1998). Preparation of HSV-DNA and Production of Infectious Virus. *Methods Mol. Med.* 10, 19–25. <https://doi.org/10.1385/0-89603-347-3:19>.
73. Lee, E.C., Yu, D., Martinez de Velasco, J., Tessarollo, L., Swing, D.A., Court, D.L., Jenkins, N.A., and Copeland, N.G. (2001). A highly efficient Escherichia coli-based chromosome engineering system adapted for recombinogenic targeting and subcloning of BAC DNA. *Genomics* 73, 56–65. <https://doi.org/10.1006/geno.2000.6451>.
74. Yu, D., Ellis, H.M., Lee, E.C., Jenkins, N.A., Copeland, N.G., and Court, D.L. (2000). An efficient recombination system for chromosome engineering in Escherichia coli. *Proc. Natl. Acad. Sci. USA* 97, 5978–5983. <https://doi.org/10.1073/pnas.100127597>.

OMTON, Volume 32

Supplemental information

TheraVision: Engineering platform technology

for the development of oncolytic viruses

based on herpes simplex virus type 1

Christina Funk, Nadja Uhlig, Zolt Ruzsics, Florentin Baur, Matthias Peindl, Sarah Nietzer, Karina Epting, Gabriele Vacun, Gudrun Dandekar, Catherine Botteron, Christian Werno, Thomas Grunwald, and Susanne M. Bailer

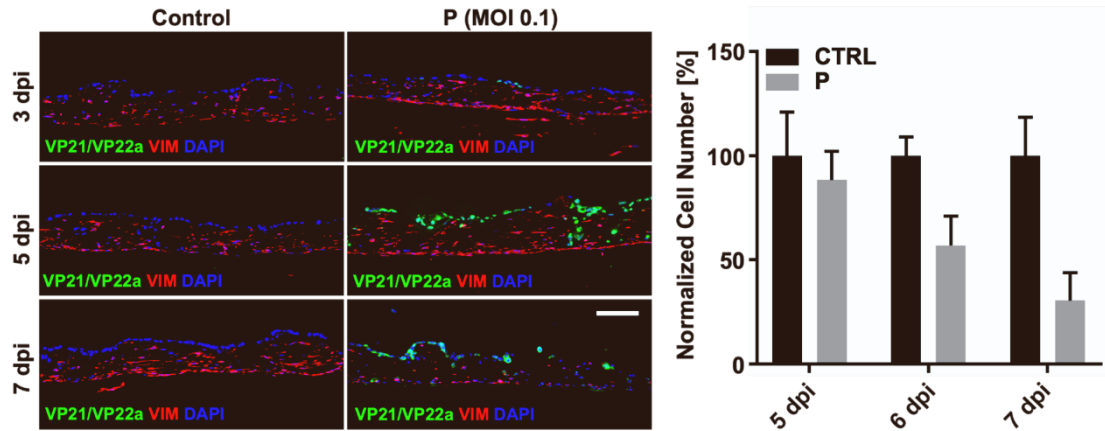


Figure S1 – Safety and efficacy evaluation of P virus in the 3D tissue tumor model

P virus does reduce cell number of tumor cells cultured on SIS muc for 14 days cells evaluated 5, 6 and 7 dpi with MOI 0.1 (mean +/-SD of 5 pictures). Immunofluorescence staining of paraffin sections illustrate that viral infection starts at the time point of 3 dpi (HSV1 proteins, VP21/VP22a, green) and also infects fibroblasts (vimentin, red) over time (5 and 7 dpi). Nuclei were visualized by DAPI staining. The scale bar corresponds to 100 μ m.

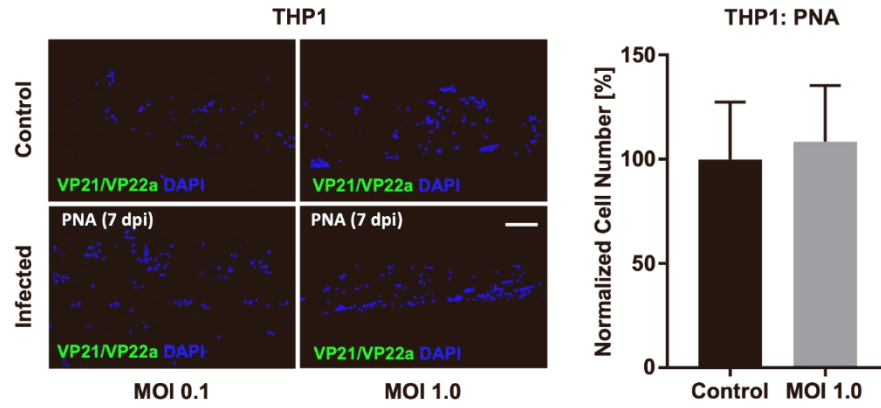


Figure S2 – Safety evaluation of PNA in the 3D tissue tumor model

Quantification of THP1 immune cells in PNA infected 3D tissue model (MOI 1.0, 7 dpi) is shown. Five pictures were analyzed for each time point. The error bars represent SD. The scale bar corresponds to 100 μm .

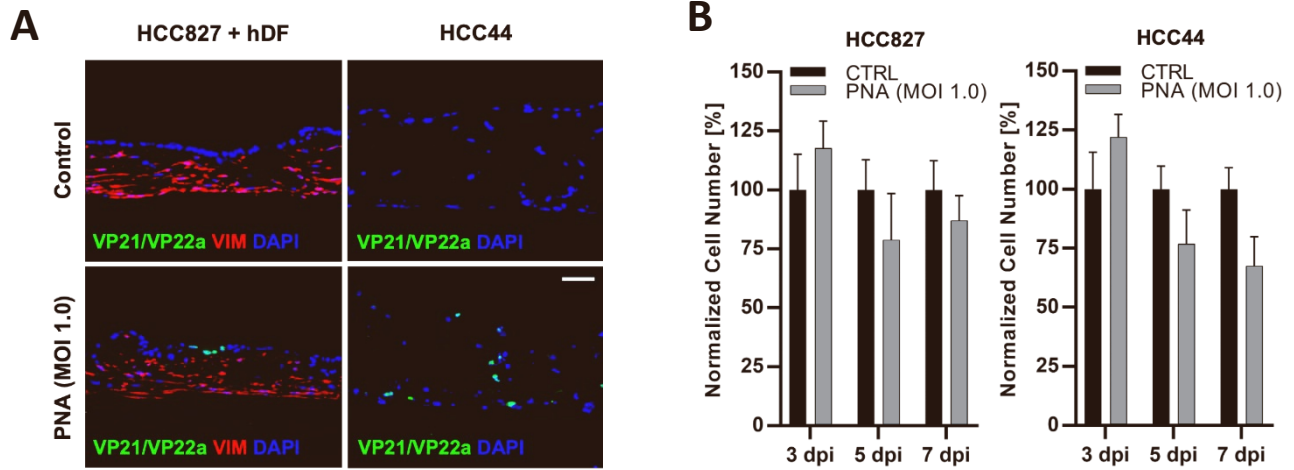


Figure S3 –Efficacy of OV in invasive tumor cells

A: 3D tissue model with either HCC827 or HCC44 cells were infected with PNA (MOI 1.0) and evaluated 7 dpi. Infection of tumor cells is illustrated in green by immunofluorescence staining (HSV1 proteins, VP21/VP22a). HDFs were visualized by staining of vimentin (red), cell nuclei by staining with DAPI. The scale bar corresponds to 100 μ m. B: Quantification of HCC827 and HCC44 carcinoma cells in PNA infected 3D tissue model (MOI 1.0) is displayed over time. Five pictures were analyzed for each time point. The error bars represent SD. White arrows indicate VP21/22a-positive tumor cells.

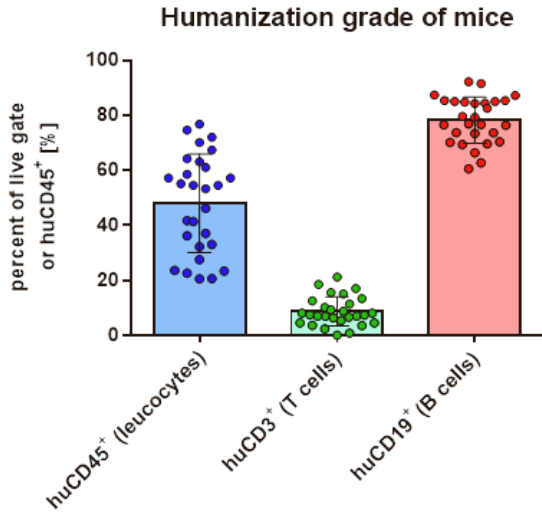
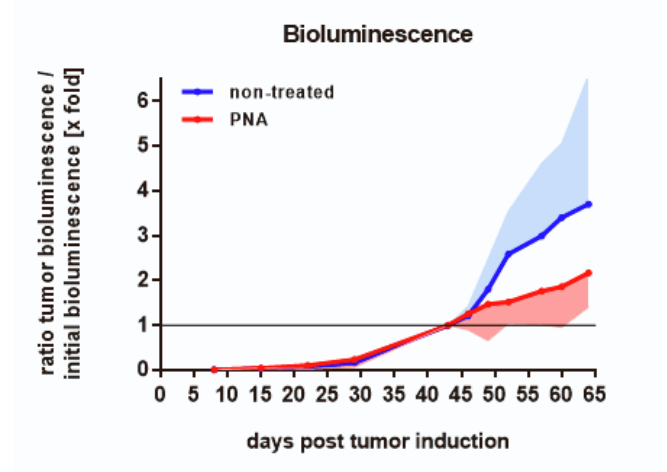
A**B**

Figure S4 – Safety of OV in mouse models

A: Examination of humanization grade in 10-12 week old NSG mice after postnatal injection of human stem cells (CD34+) by flow cytometric analysis of blood. The percentages of human leukocytes (huCD45+) of all cells after cell aggregate exclusion and distribution of human T cells (huCD3+) and B cells (CD4+) within human leukocyte fraction are shown (n=28). B: NSCLC tumor was induced in immunodeficient NSG mice using 2×10^5 HCC827Luc cells on day 0 by subcutaneous injection into the flank and intratumorally treated with $3,3 \times 10^6$ PFU of PNA on day 44. Tumor progression of non-treated (blue) or PNA treated (red) mice (n=10) compared to initial tumor volume on day 44 is shown.

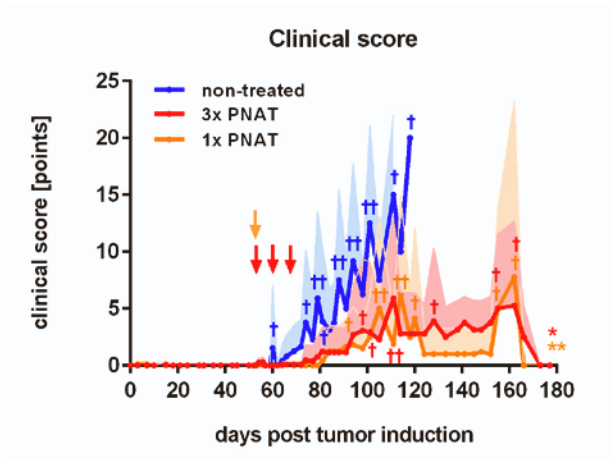


Figure S5 – Efficacy of OV in mouse models

NSCLC tumor was induced in immunodeficient NSG mice using 2×10^5 HCC827Luc cells on day 0 by subcutaneous injection into the flank and intratumorally treated once with 3.3×10^6 PFU of PNAT on day 53 (n=11, orange). Another group received PNAT intratumorally three times at 7-day intervals (n = 13, red). Additionally, a non-treated tumor group was included as control (n = 13, blue). Clinical score was determined for all animals and mean values and corresponding standard deviations of each group are shown. Statistical analysis was performed by Mann-Whitney U test in comparison to non-treated control.

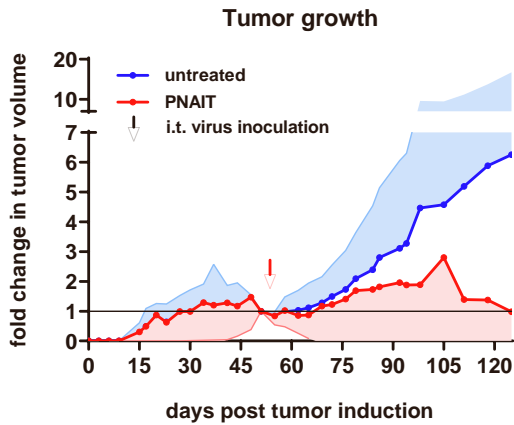


Figure S6 - Efficacy evaluation of the functionalized PNAIT virus in presence of immune cells

Immunodeficient NSG mice were humanized by intrahepatically injection of $2-4 \times 10^5$ human CD34+ hematopoietic stem cells 24-48 hours after birth (humanization status after 12 weeks: $\geq 20\%$ huCD45+ events of total CD45+ events). NSCLC tumor was induced using 2×10^5 HCC827Luc cells on day 0 by subcutaneous injection into the flank and intratumorally treated once with 1.6×10^5 PFU of PNAIT on day 55 (n = 13, red). Additionally, a non-treated tumor group was included as control (n = 11, blue). Figure 6F shows tumor progression compared to initial tumor volume on day 55.